# Bayesian luminescence dating at Ghār-e Boof, Iran, provides a new chronology for Middle and Upper Paleolithic in the southern Zagros

Maryam Heydari, Guillaume Guérin, Mohsen Zeidi, Nicholas Conard

# Bayesian luminescence dating at Ghār-e Boof, Iran provides a new chronology for Middle and Upper Paleolithic in the southern Zagros

Maryam Heydari[a,*], Guillaume Guérin[a], Mohsen Zeidi[b,c], Nicholas J. Conard[b,c]

[a] *IRAMAT-CRP2A, UMR 5060, CNRS-Université Bordeaux Montaigne, Maison de l'Archéologie, 33607 Pessac Cedex, France*

[b] *Department of Early Prehistory and Quaternary Ecology, University of Tübingen, Germany*

[c] *Senckenberg Centre for Human Evolution and Palaeoenvironment, University of Tübingen, Germany*

* Corresponding author.
*E-mail address*: mariheyd@gmail.com (M. Heydari).

## Acknowledgments

This work is part of Ph.D. thesis of M.H. financed by the Laboratoire d'Excellence Sciences archéologiques de Bordeaux (LaScArBx), a programme supported by the Agence Nationale de la Rerchere (ANR) - n◦ ANR-10-LABX-52. We are grateful to David Alba, associate editor, and three anonymous reviewers for providing constructive feedback that improved our manuscript. Sebastian Kreutzer is thanked for creating the map and running the IR-RF tests on the system at the Lux laboratory at the Université du Quebec à Montréal (Canada). We are grateful to Michel Lamothe for giving us access to his equipment for the IR-RF tests. Chantal Tribolo is thanked for her constructive comments on an earlier version of the manuscript. Hélène Valladas is thanked for irradiating two samples at the laboratory of Gif-sur-Yvette (Laboratoire des Sciences du Climat et de l'Environnement).

We are grateful to Mohammad Beheshti, the former head of research center at Iran Cultural Heritage, Handicrafts and Tourism Organization (ICHHTO), Hamideh Choubak, the former head of Iranian Center for Archaeological Research (ICAR), Monireh Kholghi, the head of international section at ICHHTO, Alireza Sardari, Ahmad Chaichi, Siamak Sarlak, Mohammad Mortezaei, Hana Bahrani Pour, and Fatemeh Farshi Jalali, at ICAR for facilitating this work and providing the necessary permits. We are also grateful to Mosayeb Amiri, the head of ICHHTO in Fars and Maghamat Mahmoudi, the head of the cultural heritage office of Rostam County for their help and facilitating the work. We thank Rasoul Boroujeni and Kourosh Alamdari, our Iranian representatives, the field crew especially Saman Hamzavi for their work in as members of the excavation team and for their

important contribution to the lab work. The excavation was funded by the Deutsche Forschungsgemeinschaft (DFG) grant CO 226/30-1.

## Abstract

Ghār-e Boof is a Paleolithic cave site in Iran well known for its rich early Upper Paleolithic Rostamian assemblages. The site is located on the edge of the Dasht-e Rostam plain in the southern Zagros. Recent excavation by the members of the Tübingen-Iranian Stone Age Research Project (TISARP) at Ghār-e Boof also recovered well-stratified Middle Paleolithic assemblages. Here we provide the first detailed luminescence chronology for the Middle and Upper Paleolithic of the site. More generally, our work is the first luminescence chronology for a Middle and Upper Paleolithic site in the Zagros Mountains region in Iran. The luminescence ages for the Upper Paleolithic of Ghār-e Boof agree with published $^{14}$C dates. We applied Bayesian models specifically designed for luminescence dating using the R package 'BayLum' to incorporate the well-established stratigraphic constraints as well as the published $^{14}$C ages with our optically stimulated luminescence (OSL) ages to improve the precision of the chronological framework. The Bayesian chronology shows a significantly improved precision of the OSL ages in particular for the upper part of the sequence where $^{14}$C ages were available. The Bayesian OSL ages for the Rostamian horizons AH III (a-b-c) and AHs IV fall in the range of 37–42 ka (68% CI). Moreover, we determined a series of dates between 45–81 ka (68 % CI) for the Middle Paleolithic strata AH IVd and AH VI. Our results point to a demographic shift in the populations responsible for the Middle Paleolithic and the Rostamian within three millennia. This major technological change accompanied by the rise of symbolic artifacts such as personal ornaments, may or may not reflect a replacement of Neanderthals by modern humans. While we are confident that the Rostamian was made by modern humans, available information does not allow us to be sure who made the local Middle Paleolithic.


**Keywords:** Luminescence chronology; Bayesian modeling; Paleolithic; Zagros Mountains; Iran.

# 1. Introduction

## *1.1. Aims of this study*

Chronological studies are an integral part of Paleolithic research to track human evolution over time. Numerous Middle and Upper Paleolithic sites were dated to establish a chronology for the dispersal of anatomically modern human (AMH) from Africa toward central Asia, in particular in the Levant (e.g., Bar-Yosef and Meignen, 2001; Grün et al., 2005; Trinkaus, 2005; Shea, 2003, 2010; Meignen, 2012; Nishiaki and Akazawa, 2018). However, further toward the east, in the vast region of the Zagros Mountains, we still lack reliable chronologies, which hampers a better understanding of the rich archaeological record of the region (Smith, 1986; Shidrang et al., 2016). While fossils of AMH are known in the Zagros Mountains (e.g., site of Wezmeh: Trinkaus et al., 2008; site of Warwasi: Tsanova, 2013), they have been poorly dated.

The Zagros Mountains have been the focus of Paleolithic studies for decades, not only to unravel the Middle and the Upper Paleolithic cultures of this region but also to decipher occupational discontinuity or transition documented in the region (e.g., Biglari, 2001; Jaubert et al., 2006; Conard and Ghasidian, 2011; Shidrang et al., 2016; Heydari-Guran and Ghasidian, 2017; Bazgir et al., 2017).

The few dated stratigraphic sequences in the Zagros Mountains rely on $^{14}C$ dating. Shanidar cave, with its rich history of study, provided radiometric ages for the Baradostian culture (Solecki 1963; Hole and Flannery, 1968; Solecki and Solecki, 1993; Becerra-Valdivia et al. 2017). Moreover, in addition to the radiocarbon sequence at Ghār-e-Boof (Conard and Ghasidian 2011; Baines et al., 2014; Becerra-Valdivia et al. 2017), $^{14}C$ dating was also applied at two sites, the Yafteh Cave (Otte et al., 2011) and the Kaldar Cave (Bazgir et al., 2017), located in the Central Zagros, to determine ages for the Upper Paleolithic in Zagros. Nevertheless, despite the few successful applications of $^{14}C$ dating, the temporal range is technically limited to the early Upper Paleolithic or very late Middle Paleolithic period (ca. 50 ka; Higham, 2011).

In this study, we present a new chronology for the site of Ghār-e Boof located at the south of the Zagros Mountains, obtained by luminescence dating. The site has yielded both Middle and the Upper Paleolithic assemblages (Conard and Ghasidian 2011; Bretzke and Conard, 2017; Conard and Zeidi, 2019; Zeidi and Conard, 2019). It is situated close to a probable passage of AMH, arriving from Africa through the south of the Iranian plateau, according to various dispersal models (Mellars, 2006; Petraglia et al., 2010; Rosenberg et al., 2011; Boivin et al., 2013; Vahdati Nasab et al., 2013).

The site of Ghār-e Boof has been excavated and studied since 2006 in the framework of the Tübingen Iranian Stone Age Research Project (TISARP). The rich and distinctive lamellar early Upper Paleolithic assemblage found during the excavation at Ghār-e Boof and during surveys at 88 sites in the Dasht-e Rostam alone stands in remarkable contrast to the Baradostian and the so-called Zagros Aurignacian. This led Conard and Ghasidian (2011) to define a new industry named the Rostamian, after the Dasht-e Rostam Plains (Conard et al., 2013). The Upper Paleolithic sequence of the site was already dated with $^{14}$C dating in several earlier studies (Conard and Ghasidian, 2011; Baines et al., 2014; Becerra-Valdivia et al., 2017). These results were refined using Bayesian modeling, leading to the earliest Upper Paleolithic settlement between 41,950–39,850 cal BP (68% credible interval [CI]; Becerra-Valdivia et al., 2017). Ghasidian's doctoral research resulted in detailed presentations of the cultural sequence of the Rostamian from Ghār-e Boof (Ghasidian, 2014; Ghasidian et al., 2017) based on the first two seasons of excavation in 2006 and 2007. Fieldwork by the TISARP team in 2015 and 2017 extended the stratigraphic sequence to bedrock and uncovered multiple Middle Paleolithic find horizons (Bretzke and Conard, 2017; Conard and Zeidi, 2019; Zeidi and Conard, 2019).

Below, we provide details of the luminescence dating for the Middle and Upper Paleolithic sequence of the site, and we compare the obtained luminescence ages of the Upper Paleolithic with those available $^{14}$C ages. We present the first luminescence-based chronology for the Middle Paleolithic period in the south of the Zagros Mountains. Moreover, our study goes beyond a simple Middle and Upper Paleolithic luminescence chronology for the Zagros Mountains: we also deployed Bayesian modeling as implemented in the R (R Core Team, 2019) package 'BayLum' (Combès et al., 2015, Combès and Philippe, 2017; Philippe et al., 2018) to incorporate all available chronological

77 data (optically stimulated luminescence [OSL] and $^{14}C$ ages) for the site of Ghār-e Boof, to render a
78 precise chronology covering both the Middle and the Upper Paleolithic periods. The advantages of
79 such incorporation in Bayesian School will be discussed.
80

81 ### *1.2. Environmental setting*

82 The Dasht-e Rostam region is located in the south of the Zagros Mountains in the northwest of
83 the Fars Province. The province stretches mainly across the Zagros Folded belt. Most of the
84 elevations of this belt are comprised of parallel limestone anticlines, which are generally oriented
85 from northwest to southeast (Brookes, 1989; Stöklin and Navabi, 1973). The topography of this area
86 is diverse with various geomorphological features such as mountains ranging from 700 to 2500 m
87 a.s.l., valleys, rivers, and plains (Heydari-Guran, 2014). The area is known to be semiarid to arid, but
88 the presence of the permanent Fahliyan River (Fig. 1) alongside more than 50 springs and seasonal
89 rivers, like Shiv and Solak form a local wetland (Heydari-Guran, 2014). The climate of this region
90 belongs to the mild temperature zone (Bobek, 1968; Ganji, 1968).
91 The geological context in this area comprises the Miocene to the Quaternary, and the Jurassic to
92 the Oligocene (Heydari-Guran, 2014). The rocks of this region are mainly composed of limestone,
93 dolomite and argillaceous limestone, which is a normal pattern for the Zagros Mountains (Ghasidian,
94 2014; Motiei, 1993).
95 Members of the Tübingen-Iranian Stone Age Research Project (TISARP) conducted survey in the
96 Dasht-e Rostam and identified numerous Paleolithic sites in the form of open-air sites, rock shelters,
97 and caves. Study of these lithic artifacts assemblages showed that they mainly originate from the
98 Upper Paleolithic (Conard and Ghasidian, 2011; Heydari-Guran, 2014). According to the distribution
99 of the discovered lithic artifacts from the surface, the region was classified into divided small zones
100 (microhabitats; Heydari-Guran, 2014). One of those zones, which exhibits the highest concentration
101 of lithic artifacts, is the Yagheh Sangar corridor. The pass is situated in the middle of the Dasht-e
102 Rostam, and it connects plains of Dasht-e Rostam I and Dasht-e Rostam II (Fig. 1). This corridor

encompasses several caves, rock shelters, and open-air sites, which contains ca. 33 % of the known Paleolithic sites in the Dasht-e Rostam plains (Heydari-Guran, 2014). The cave of Ghār-e Boof, which is located at an altitude of 905 m a.s.l., 40 m above the valley bottom, is one of these Paleolithic sites, in the center of the Yagheh Sangar corridor.

The area inside of the cave is ca. 60 $m^2$, with a ceiling height of ca. 8 m (Fig. 1). The Fahlian River is located 5 km at the south of the cave, and the seasonal Solak stream is situated within 200 m at the northeast of the cave. Several large boulders at the entrance of the cave protect the deposited sediments inside the cave from being washed away by erosional processes (Conard and Ghasidian, 2011, Ghasidian, 2014). These preserved sediments distinguish the site of Ghār-e Boof from the other Paleolithic sites in the region, providing a unique potential for further systematic investigations. Surface studies yielded 436 lithic artifacts, categorized by the presence of flakes, blade and, especially, bladelets and bladelet cores (Conard and Ghasidian, 2011; Ghasidian, 2014). The chert from the river of Fahlian was the main source of raw material for producing lithic artifacts.

In the following, the observed layers are identified based on geological horizons (GH) and archaeological horizons (AH). Besides, both GH and AH refer to identical layers but were investigated using different approaches.

Stratigraphy The overall sequence at Ghār-e Boof is comprised of nearly 6 m of well-stratified deposits. The geological horizons 1 and 2 (GH1, GH2) at the top of the profile are associated with the Holocene. GH 2 encompasses two sublayers (GH 2a and GH 2b). The bottom of GH 2 (GH 2b) contains limestone cobbles with sizes from 5 to 25 cm in the north and the center of the profile (western wall; Fig. 2). These cobbles separate the Holocene layers from the Pleistocene layers, which start from GH 3 onwards (Ghadisian, 2014).

GH 3, with thicknesses ranging from 10 to 65 cm in different parts of the cave, often contains ashy silt sediments with colors from yellow-brown to light gray. Fragments of limestone are present in this layer. Sublayers GH 3a and GH 3b underlay GH 3 with a thickness of ca. 15 cm and ca. 60 cm, comprised of medium brown ashy silt and dark brown silt, respectively. Both sublayers contain

abundant lithic artifacts, faunal remains and pieces of charcoal. Continuing downward, GH 4 consists of yellow-gray silt with a thickness of ca. 15 cm. The density of limestone fragments in this layer is higher than in GH 3. GH 4a with a thickness of ca. 30 cm, is characterized by a mixture of light yellow-brown silt and limestone fragments smaller than 5 cm. GH 4b, that is darker in color than GH 4a, and contains light brown silt and pieces of limestone in lower concentration than GH 4a. Finally, GH 5 and GH 6, which correspond to about 2.5 m of deposits overlying the bedrock (Fig. 2), are comprised of light brown to gray silty sediments with a large amount of limestone clasts (Conard and Zeidi 2019; Zeidi and Conard 2019).

Archaeological finds The archaeological horizons AH I and AH II contain ceramic and pottery sherds, which are attributed to the historical period (Conard and Ghasidian, 2011). AH III yielded the richest archaeological materials, not only because of the high concentration of lithic artifacts but also because of fragmented but well-preserved animal bones. The botanical remains preserve what appears to be an exceptional record of early dietary plant use during the Rostamian (Baines et al. 2014). The lithic artifacts from AH III, which are rich in bladelets and tools made on bladelets, make Ghār-e Boof the type locality for the Rostamian (Conard and Ghasidian, 2011, Conard et al., 2013; Ghasdian, 2014). Moreover, many perforated shells of various species from AH II b to AH IV were used as personal ornaments (Conard and Ghasidian, 2011; Ghasidian, 2014; Conard and Zeidi, 2019).

The concentrations of lithic artifacts in the Middle Paleolithic strata of AH IVd-VI are low compared to the extremely rich Rostamian deposits. These layers also contain large amounts of charred botanical remains as well as faunal remains that are currently under study. The Middle Paleolithic assemblages excavated in 2015 and 2017 have thus far only been published in preliminary reports (Bretzke and Conard, 2017; Conard and Zeidi, 2019; Zeidi and Conard, 2019).

# 2. Materials and methods

## *2.1. Sampling*

Fourteen sediment samples were taken from the south of the western and northern walls (Fig. 2) starting from AH IIIb on top of the sequence to AH VI right above the bedrock. To protect the stability of the profile, we avoided hammering and collected the samples in opaque bags at night using orange light. For the sampling, first, we cleaned each sampling location and removed a sediment layer of ca. 5 cm to avoid sampling weathered sediments subject to recent long-term exposition to light and air. Then, we collected the sediments by digging into the profile.

## *2.2. Sample preparation*

Sample preparations were carried out following commonly accepted luminescence sample preparation procedures (Preusser et al., 2008) under subdued orange light conditions appropriate for luminescence dating (sodium vapor lamp, ca. 589 nm). Wet sieving was performed to extract grains between 41 to 60 µm. We have selected this grain-size because it represents the dominant fraction of the material available in (relative) abundance, and the fraction could be prepared in a reasonable amount of time. The samples were then treated with HCl (10% and 35%) to dissolve carbonates until no more reaction was observed. The samples were then treated with $H_2O_2$ (30%) for one week to eliminate organic materials. Then, we divided the prepared sediments into two groups: Group 1 was treated using HCl (35 %) at 65 °C for 3 h to remove the iron coating. We retained this part of the so-prepared samples (polymineral) for infrared stimulated luminescence (IRSL) measurements. Group 2 was soaked with a mixture of 90% hexafluorosilicic acid ($H_2SiF_6$, 37%) plus 10% nitric acid ($HNO_3$ 68%; cf. Frayret et al., 2006 for the procedure) for one week to obtain purified quartz grains. This procedure was followed by another wash in HCl (15%) overnight to remove remaining calcium fluorides. Finally, wet sieving was applied again to discard any remaining grains from the mineral group of feldspar as well as removing any aggregated quartz with the size of

177 less than 41 µm. The amount of quartz grains for sample GB12 was negligible. Therefore, we could
178 not perform any measurements on quartz for this particular sample.
179

180 *2.3. Instrumentation and source calibration*

181 OSL (Huntley et al., 1985) and IRSL (Hütt et al., 1988) were carried out on two Freiberg
182 Instruments lexsyg SMART TL/OSL systems (Richter et al., 2015). For estimation of the equivalent
183 dose ($D_e$) of the quartz grains, we used a system equipped with five blue LEDs (458 Δ 10 nm,
184 maximum 70 mW $cm^{-2}$) and five infrared LEDs (850 Δ 3 nm, max. 300 mW $cm^{-2}$). The stimulation
185 power was set to 40 mW $cm^{-2}$ for blue and 100 mW $cm^{-2}$ for infrared during continuous wave (CW)
186 stimulation. For estimating the $D_e$ of the polymineral grain, we employed another system, equipped
187 with ten green LEDs (525 Δ 20 nm, maximum 70 mW $cm^{-2}$) and five infrared LEDs (850 Δ 3 nm,
188 maximum 300 mW $cm^{-2}$) set to 100 mW $cm^{-2}$ (infrared) during continuous wave (CW) stimulation.
189 The heating rate for TL signal measurements for both blue-OSL and IRSL measurements was 5 °C/s.
190 Luminescence was detected through a UV filter set for blue-OSL measurements (Schott BG 3, 3 mm
191 and Delta BP 365/50 EX) and a blue-violet filter combination for IRSL measurements (Schott BG 39, 3
192 mm and AHF-BL HC 414/46 and Schott NG 11, 1 mm) in front of a Hamamatsu H7360-02
193 photomultiplier tube (PMT). The two readers were equipped with a $^{90}Sr/^{90}Y$-source, which were
194 specifically calibrated for our samples due to their small grain size (41–60 µm). We used grains from
195 sample GB4 for calibration with quartz grains as well as calibration with polymineral fraction. The
196 samples were first bleached following the procedure of dose recovery test (see Section 2.4) and then
197 were irradiated with an external $^{137}C$ gamma-source (Valladas, 1978) in the laboratory of Gif-sur-
198 Yvette (Laboratoire des Sciences du Climat et de l'Environnement). The quartz grains and the
199 polymineral both received a gamma-dose of 53 Gy. We measured the given dose using a single
200 aliquot regenerative (SAR) dose protocol (Murray and Wintle, 2000) with the same set up as for our
201 measurements (see below). The result showed that the two luminescence readers delivered ca. 8.52

Gy $min^{-1}$ (reader used for the quartz measurements) and 9.96 Gy $min^{-1}$ (polymineral) to grains of 41–60 µm.

Several hundred grains, either quartz or polymineral, were mounted on the stainless steel cups using silicon oil and a mask of diameter 1 mm (small size). We measured 30 aliquots per sample for the quartz grains and 15–16 for the polymineral fractions.

For additional radiofluorescence (RF) test measurements in Bordeaux, we employed the system used by Frouin et al. (2017). Radiofluorescence spectrometry measurements were carried out on the lexsyg research (Richter et al., 2013) system of the Lux laboratory at the Université du Quebec à Montréal. The system is similar to the system in Bordeaux but equipped with an Andor SR-163 spectrograph on conjunction with an Andor DU420A-OE CCD camera connected via a glass fiber to the measurement position. The system was wavelength calibrated, and efficiency calibration relied on technical data relayed by the manufacturer.

### *2.4. Luminescence signal measurements*

We measured luminescence signals of the quartz and polymineral fraction to determine the corresponding equivalent doses. These procedures enable us to compare the final obtained ages from different minerals and protocols and increase the confidence in the luminescence chronology for Ghār-e Boof.

Quartz optically stimulated luminescence We applied a SAR protocol to the quartz samples to determine the equivalent doses ($D_e$). Quartz blue-OSL signal (detected in the UV wavelength) consists of several signal components (Bailey et al., 1997). However, the SAR protocol is preferentially employed for the fast decaying signal component, the so-called fast component, bleachable within a few seconds (Wintle and Murray, 2006). Therefore, the first step of measurement was to verify whether quartz samples of the site of Ghār-e Boof were dominated by the fast decaying component or not. We compared one sample from the site (GB1) with the calibration quartz (Risø, batch 90; Hansen et al., 2015), which is known to be dominated by the fast

component, using blue CW-OSL, and the corresponding luminescence signals were measured in the UV. Both signals were then transformed into the pseudo-linearly modulated-OSL, following Bos and Wallinga (2012)—for results see Section 3.1.

The OSL signal was measured at 125 °C for 40 s following a preheat for 10 s. The test-dose was measured following a cut heat. We employed the Analyst software v. 4.53 (Duller, 2015) for determining the equivalent doses ($D_e$). Regenerative dose points were set at 22, 44, 88, 176, and 352 Gy following a test dose of 22 Gy for regeneration dose 1 to 5 (R1 to R5). We calculated the signal intensity based on the initial 0.2 s of stimulation, and the background was estimated from the last 10 s. An exponential plus linear function was used for fitting the dose-response curves. After delivering the largest regenerative dose point in the SAR sequence (R5), the samples were given a zero dose (R6) to measure the potential effect of charge transfer due to the previous irradiation or stimulation (Wintle and Murray, 2006). After recuperation, the first regenerative point cycle was repeated (R7) to check the efficiency of correction for sensitivity changes. To account for the possibility of potential contamination of the quartz grains by feldspars, we applied an IR depletion ratio test (Duller, 2003) administrating the same dose as for the first regenerative dose at the end of each SAR cycle (R8).

To monitor a dependency of the $D_e$ upon the preheat temperature, the preheat plateau test was carried out for sample GB4. The minimum preheat temperature was set to 200 °C, then increased by 20 °C at each step to reach a final temperature of 300 °C. We kept the distance between the preheat and the cut-heat temperature constant at 40 °C.

Additional dose recovery tests were performed on samples GB4 and GB8. The natural signals were first bleached for 100 s in a solar simulator, and then the procedure was followed by a pause of 3 h before the samples were bleached again for another 100 s to eliminate potential charge transfer from the shallow traps to the main trap (325 °C trap). Samples GB4 and GB8 received doses of 57 Gy and 67 Gy (close to their paleodose) respectively, using beta-source inside the luminescence reader, then the given doses were measured using the SAR protocol.

Polymineral fraction and the infrared stimulated luminescence Feldspar has been extensively used in luminescence dating. Stimulation of this mineral with an infrared wavelength produces the IRSL signal (Hütt et al., 1988), usually measured in the blue-violet wavelength range, which has several advantages over the quartz OSL signal measured in the UV. The IRSL signal saturates at higher doses compared to the quartz OSL, which leads to the extension of the dating range limitation. Moreover, IRSL signal of potassium feldspar is brighter and usually resulting in lower statistical uncertainties (e.g., Li and Li, 2011). However, IRSL signal suffers from athermal fading (e.g., Wintle, 1973; Spooner, 1992), e.g., an unwanted loss of the signal of interest. To overcome this problem, several concepts have been proposed either to correct for fading (e.g., Huntley and Lamothe, 2001) or to use signals with a lower rate of fading (Thomsen et al., 2008, 2011; Thiel et al., 2011). These investigations showed that an elevated temperature IRSL signal displays low or even negligible fading (Thomsen et al., 2011; Li and Li, 2011). These concepts resulted in a series of measurement protocols measuring the IRSL signal at elevated temperatures, e.g., 290 °C following IRSL at 50 °C, the so-called post-IR IRSL 290 °C ($pIRIR_{290}$) protocol (Buylaert et al., 2012). The $pIRIR_{290}$ signal is believed not to require any fading correction for the doses <400 Gy (Li and Li, 2012; Zhang and Li, 2020). Hence, this signal was measured for all of the samples using the protocol proposed by Buylaert et al. (2012). The setting of this protocol is listed in Supplementary Online Material (SOM) Table S1.

First, dose recovery tests were carried out on two samples: one sample from the top of the sequence (GB1) and the other one from the bottom of the sequence (GB14). The samples were first bleached for 72 h under the solar simulator then the residual doses were measured, which were 3 Gy for sample GB1 and 4 Gy for sample GB14. In the following, samples GB1 and GB14 received doses of 65 Gy and 124 Gy using beta-source inside the luminescence reader, then the given dose was measured using the $pIRIR_{290}$ protocol. The residual doses were subtracted from the measured dose.

## *2.5.* Dose rates

Energy available to luminescence dating is stored in natural minerals (e.g., quartz) mainly due to the emission of alpha and beta particles as well as gamma photons from natural radionuclides in the surrounding sediment along with dose contributions from high-energetic cosmic rays (Aitken, 1985). Additionally, radionuclides inside potassium feldspar and quartz grains result in an internal dose rate contribution. However, the internal dose rate of quartz grains is often negligible in comparison with the internal dose rate of potassium feldspar grains (Mejdahl, 1987; Huntley and Baril, 1997).

The main sources of external radioactivity are nuclides of the U and Th decay chain, as well as K. For our study, the concentration of these radioelements was determined using high-resolution, low-level background gamma-ray spectrometry (Guibert and Schvoerer, 1991). We have assumed that the true beta-dose rate arose from sediment with the grain size less than 2 mm and between 2mm to 1 cm after Martin (2015) and Tribolo et al. (2017). For our samples, however, the amount of grains between 2mm and 1 cm was negligible compared to the fraction less than 2 mm. Thus, the sediment samples were first sieved using a mesh size of 2 mm; then the smaller size fraction was packed and sealed in boxes of 12 $cm^3$. Storage time of at least four weeks ensured a radioactive equilibrium between $^{222}Rn$ and its daughters (Guibert and Schvoerer, 1991). The obtained equivalent concentrations of U, Th and K were converted to dose rates using the factors tabulated by Guérin et al. (2011). The attenuation of alpha and beta particles was corrected after Guérin et al. (2012). We applied alpha-efficiency values (a-values) of 0.03 ± 0.01 after Mauz et al. (2006) to calculate the alpha-dose rate for the quartz grains. For the polymineral fractions, we calculated the average alpha-efficiency and its standard deviation (0.093 ± 0.013) from values presented for $pIRIRSL_{290}$ in Schmidt et al. (2018).

Based on a granulometric analysis (see SOM Fig. S1 as an example) and derived pore volume data, we approximated that a value of 15 ± 6 % would best represent the past water content. This value was increased to 20 ± 8 % for the last two samples (GB13 and GB14), which were taken from GH 6 because of markedly higher water content observed at this particular layer. The uncertainty on

water content was set to 40%; this relatively large value was chosen to cover a wider range of water content values. To correct dose rates for the water content, we applied values tabulated in Aitken (1985), Nathan and Mauz (2008) and Guérin and Mercier (2012) for alpha and beta particles, and gamma photons respectively.

The internal dose rate for the quartz grains was calculated using nuclide concentration values from Vandenberghe et al. (2008). For feldspar grains in the polymineral fractions, we assumed an internal K concentration of 10 ± 2% after Smedley et al. (2012), and accordingly, we estimated the internal dose rate (Rb was taken into account with a concentration of 370 ± 74 ppm following Mejdahl, 1987) using the conversion factors of Guérin et al. (2011) and corrected for the self-dose fraction after Guérin et al. (2012).

The in situ gamma dose rate was measured for nine samples (GB1 to GB9) using $Al_2O_3$:C chips following the procedure of Kreutzer et al. (2018). The chips were heated to 350 °C for 10 min before being dispatched. Each aluminum tube contained three chips. The tubes stayed in the sediment 720 days (within 5 cm horizontal distance from the location of the corresponding sample). For samples GB10 to GB14, the gamma-dose rates were derived from radionuclide concentrations of K, U and Th obtained by gamma-ray spectrometry (see Section 2.6).

The cosmic-dose rates were calculated after Prescott and Stephan (1982) and Prescott and Hutton (1994). For the calculation, we used a self-written Microsoft Excel™ sheet. It was designed to estimate the cosmic dose rate from four different directions, two sections from the cave entrance and two other sections form the rear of the cave. For each section, the cosmic dose rate was estimated based on nine subsections (in the spherical coordinate system from 0° to 10°,10° to 20° to finally 80° to 90°). We then summed the dose rate estimated from each 10° representing the dose rate of each section. The final dose rate is the sum of the dose rate from all four sections. For estimating the overall uncertainty, we have employed 10% after Prescott and Hutton, (1994) on the final dose rate estimation. To calculate the total dose rate ($D_r$), we used a self-written Microsoft Excel™ sheet.

Radioactive disequilibrium Equilibrium in the U decay chain is an underlying fundamental assumption to estimate the dose rate. However, due to the mobility of some of the radionuclides in a particular environmental setting, radioactive disequilibria can be observed. Typical sources of radioactive disequilibria are: (1) $^{234}U$ (preferentially over $^{238}U$) can form water-soluble oxidation compound (Krbetschek et al., 1994) that might be transferred and accumulated in other layers; (2) Ra is soluble and chemically active, and can be leached; (3) entrance of soluble $^{210}Pb$ in soil water; and (4) loss of $^{222}Rn$ (gas) due to large pores. One of the typical ways to monitor the possibility of disequilibria in $^{238}U$ decay chain is to estimate the effective $^{238}U$ content from the top of the chain (pre-$^{226}Ra$) and from the bottom (post-$^{226}Ra$), which accounts for the potential high chemical mobility of $^{226}Ra$ (Guibert et al., 2009). To better illustrate the probable radioactive disequilibrium in the $^{238}U$ decay chain, the effective $^{238}U$ concentrations from the top and the bottom of the U-series were normalized to $^{232}Th$, which is believed to be chemically immobile, to provide a better indicator of radionuclides movement in $^{238}U$ following the approach of Guibert et al. (2009). The figure is shown in the results section.

### *2.6. Combining quartz ages with the radiocarbon ages in 'BayLum'*

The R (R Core Team, 2019) package 'BayLum' provides an environment for Bayesian data analysis in luminescence dating (Philippe et al., 2018; Christoph et al., 2019; for an application see Heydari et al., 2020). However, 'BayLum' is also capable of combining available chronological information, in particular, stratigraphic constraints and $^{14}C$ dates with OSL ages to improve luminescence chronologies. This may be considered as the most important advantage of performing data analysis in a Bayesian framework (although gains in precision and accuracy have already been demonstrated when using the models implemented in 'BayLum'; Heydari and Guérin, 2018) since it had the potential to lead to more precise chronologies (e.g., Rhodes et al., 2003; Millard et al., 2006; Guérin et al., 2015). Integrating OSL ages with $^{14}C$ dates for one specific site in 'BayLum' can reduce the effect of shared systematic errors between the samples in OSL dating. Systematic errors affecting

series of OSL ages can be modeled using the concept of the covariance matrix, which is named theta matrix in 'BayLum' (Combès and Philippe, 2017). The uncertainty on the calibration of gamma-ray spectrometry, for measuring beta and gamma dose rate as well as the uncertainty on the beta-source of the luminescence reader are the main sources of uncertainty inserted into the theta matrix for our study (for full implementation see Heydari et al., 2020). However, for 11 out of 13 quartz samples we employed in situ gamma dose rate measurements while for the two last samples, we used values derived from gamma-ray spectrometry (see Section 4.2). We did not consider the systematic source of uncertainty for the alpha dose rate due to its low contribution compared to the total external dose rate (see Section 3.2).

The input for running the model in 'BayLum' is raw data in the form of BIN/BINX-files and the associated information such as channel integrals, the dose rate of the luminescence reader and the environmental dose rate. We assumed that the Gaussian distribution is a representative model to illustrate the equivalent doses (Guérin et al. 2017; Heydari and Guérin, 2018). The uncalibrated $^{14}C$ ages with the corresponding uncertainty published in Conard and Ghasidian (2011), Baines et al. (2014) and Becerra-Valdivia et al. (2017) were also combined with the OSL ages and calibrated using IntCal13 (Reimer et al.,2013). For all calculations, the stratigraphic order constrained the modeling.

# 3. Results

## *3.1. Equivalent dose*

Quartz equivalent dose The results of transformed signals into the pseudo-linearly modulated-OSL from the calibration quartz and sample GB10 are shown in SOM Figure S2. The perfect match of the two curves indicates that the fast signal component dominates the quartz of the samples of Ghār-e Boof.

In the SAR protocol the normalized recuperation signal to the natural signal was always less than 5% for our samples. The recycling ratio (R7/R1) was less than one, and the average of these ratios for

our samples ranged from 0.82 ± 0.00 (for sample GB7) to 0.87 ± 0.02 (for sample GB6). The averages of these ratios for all samples are listed in SOM Table S2. The average of the IR depletion ratios (R8/R7) for each sample ranged from 0.977 ± 0.008 to 0.991 ± 0.003. These results indicate that the quartz samples were not contaminated with feldspar.

Typical dose-response curves and luminescence signals from quartz are shown in Figure 3a as examples. We have also illustrated the TL curves from blue-OSL to visualize the preheat.

The result of the preheat measurements is shown in SOM Figure S3; each point represents the average of $D_e$ after measuring 5 aliquots. The figure illustrates a plateau from 220 to 260 °C, indicating that these temperatures can be used for preheat. We selected a preheat temperature of 260 °C for our measurements. The dose recovery ratio resulted in 1.12 ± 0.04 and 1.12 ± 0.05 (average of three measured aliquots). We tried to modify the preheat and the cut-heat temperatures to improve the dose recovery ratio and found that a preheat temperature of 280° C and test dose cut heat of 260°C (henceforth 280–260 °C) led to the best dose recovery ratios of 1.01 ± 0.01 and 1.00 ± 0.03 for GB4 and GB8 (average of three measured aliquots). We also performed a preheat plateau test for this protocol on sample GB8. The preheat varied from 220°C to 280°C with the cut heat set to 20 °C less than the preheat at each step.

The result of this preheat test is shown in SOM Figure S4. This figure illustrates that the measured $D_e$ using the 280–260 °C protocol appears not to be located in the plateau. Therefore, we continued our measurement using 260–220 °C protocol. However, we determined the equivalent doses using the 280–260 °C protocol for three samples GB1, GB4 and GB8 and divided the obtained $D_e$ from the 260–220 °C protocol to the corresponding $D_e$ obtained derived from the 280–260 °C protocol. The ratios were 1.00 ± 0.03, 1.00 ± 0.03 and 1.01 ± 0.03 for samples GB1, GB4 and GB8 respectively, i.e., indistinguishable from unity. Therefore, we concluded that for our samples, the dose recovery test is not a good representative to test the suitability of the SAR protocol parameters. This observation is in agreement with Guérin et al. (2015), who showed that dose recovery might not be a strong indicator of the accuracy of the measurement protocol settings.

Polymineral equivalent dose We obtained dose recovery ratios of 0.99 ± 0.02 for sample GB1 and 0.97 ± 0.3 (average of three measured aliquots) for sample GB14 and thus within 10% of unity. The proportions of the test dose to the given dose were 44% for sample GB1 and 23% for sample GB14. These results agree with the findings by Colarossi et al. (2017), who suggested that the ratio of the test dose to the given dose in the $pIRIR_{290}$ signal should not be less than 15%. Besides the average of recycling ratios for our samples here ranged from 0.99 ± 0.06 (for sample GB6) to 1.05 ± 0.01 (for sample GB5). Contrary to quartz samples, recycling ratios for polymineral were within 5% of unity. The average of the recycling ratios (for consistency with blue-OSL measurements) for all samples are summarized in SOM Table S3.

Typical dose-response curves and luminescence signals from sample GB1 are shown in Figure 3b as examples. We have also illustrated the TL curves from $pIRIRSL_{290}$ to visualize the preheat.

Scatter in the equivalent dose distributions The distributions of the $D_e$ for both, quartz and polymineral, are exemplarily displayed for samples GB3 and GB14 as Abanico plots (Dietze et al., 2016) in Figure 4a–d. The $D_e$ distributions for all samples are provided in the SOM Figures S5 and S6. Additionally, we have calculated the overdispersion for each $D_e$ distribution (SOM Table S4) after Galbraith et al. (1999). The $D_e$s are quoted as arithmetic average ± the standard error of the mean. The $D_e$s of the quartz grains and polymineral fractions ranged from 55 ± 1 to 104 ± 3 Gy and from 65 ± 2 to 124 ± 3 Gy, respectively (Table 3).

To justify the use of the arithmetic average for calculating the central dose, despite observing the scatter within aliquots (Fig. 4; for complete version see SOM Figs. S5 and S6), we have, additionally, calculated the central dose using the average dose model (ADM) after Guérin et al. (2017). In this model, the uncertainty on each $D_e$ is considered to provide the final central dose. These results are listed in SOM Table S5. This table shows that the arithmetic average and the ADM lead to almost identical results. Thus, the arithmetic average is an appropriate measure for this dataset despite the observed scattering between aliquots.

### *3.2. Dose rate*

The equivalent concentrations of U, Th and K, as well as the calculated external and total dose rates, are shown in Table 1 and 2, respectively. The internal dose rate for quartz and polymineral grains were estimated using DRAC v. 1.2 (Durcan et al., 2015) resulted in 0.01 ± 0.00 and 0.18 ± 0.04 Gy $ka^{-1}$. The external alpha dose rates varied between 0.04 ± 0.01 and 0.06 ± 0.01 Gy $ka^{-1}$ for the quartz grains and between 0.13 ± 0.02 and 0.20 ± 0.03 Gy $ka^{-1}$ for the polymineral fractions. The external beta dose rates ranged from 0.53 ± 0.02 to 0.89 ± 0.05 Gy $ka^{-1}$.

The in situ gamma dose rate for samples GB1 to GB9 varied between 0.40 ± 0.03 to 0.49 ± 0.03 Gy $ka^{-1}$, which is in good agreement within uncertainties with the corresponding gamma-dose rates derived by laboratory gamma-ray spectrometry, which ranged from 0.35 ± 0.01 to 0.47 ± 0.02 Gy $ka^{-1}$ (for samples GB1 to GB14). The final dose rate for the quartz grains ranged from 1.02 ± 0.03 to 1.55 ± 0.06 Gy $ka^{-1}$ and correspondingly for potassium feldspar ranged from 1.29 ± 0.05 to 1.81 ± 0.07 Gy $ka^{-1}$.

To address figuratively possible radioactive disequilibria, we have plotted the ratio of effective U concentration derived from the top of the chain (pre-$^{226}$Ra) as well as from the bottom of the chain (post-$^{226}$Ra) divided by $^{232}$Th as it was mentioned in Section 2.5. In Figure 5, most of the samples lie close to the equilibrium line. However, the effective $^{238}$U concentrations estimated from the top of the chain are higher (from ca. 1.2 times to a maximum of 1.9 times) than the corresponding contents from the bottom of the chain for samples GB2, GB4, GB7, GB10, GB13, and GB14. Unfortunately, it is not straightforward to distinguish whether the source of disequilibria can be attributed to the top or from the bottom of the U chain. Hence, we have decided to calculate the average of the effective $^{238}$U from the top and the bottom of the chain for samples GB2, GB4, GB7, GB10, GB13, and GB14 and presented the dose rate according to the average. However, if we assumed that the disequilibria happened recently in the top of the chain then considering the lower effective U concentration from the bottom, would lead to older ages, from 1% to a maximum of 7%. Likewise calculating the ages from the effective U concentration from the top of U chain compared to the average would lead to

460 younger ages, from 1% to a maximum of 6%. However, these differences do not have a significant
461 effect on the overall Paleolithic interpretation.
462

463 ### *3.3. Quartz and polymineral ages*

464 Blue-OSL ages from the quartz samples alongside $pIRIR_{290}$ ages from the polymineral samples
465 within their standard errors (68% confidence interval) are shown in Figure 6. The figure also presents
466 the calibrated $^{14}C$ ages after Baines et al. (2014) and Becerra-Valdivia et al. (2017)— the calibrated
467 ages are taken from Ghasidian et al. (2019). We split those ages into two groups associated with the
468 year of their publication: $^{14}C$ (2014) and $^{14}C$ (2017) in the legend of Figure 6. The names of
469 archaeological layers in which the samples were taken are displayed next to each sample's name.
470 At first glance, a perfect agreement between the quartz ages and the polymineral ages is
471 observed for almost the entire sample set. Both quartz and polymineral ages smoothly increase with
472 depth. Moreover, the $^{14}C$ ages agree with the luminescence ages from the top of the sequence.
473

474 ### *3.4. Infrared radiofluorescence tests on the polymineral fraction*

475 We employed infrared radiofluorescence (IR-RF; Trautmann et al., 1998, 1998) using the protocol
476 suggested by Frouin et al. (2017) on two polymineral samples (GB2 and GB14). Unfortunately, the
477 determined $D_e$s significantly overestimate those values obtained with the $pIRIR_{290}$ protocol (values
478 not shown). To rule out insufficient luminescence signal bleaching as a potential (but here unlikely)
479 cause for this overestimation, we additionally recorded RF spectra (see SOM Fig. S7 as an example
480 for sample GB2) using again the protocol by Frouin et al. (2017). These measurements revealed that
481 the RF spectra are dominated by a strong red emission, while the here relevant IR emission is not
482 distinguishable from background noise, i.e., the polymineral samples from Ghār-e Boof are
483 unsuitable for IR-RF dating; thus, this approach was not further followed up.
484

### *3.5. Bayesian ages*

Figure 7 illustrates the result of quartz ages combined with the $^{14}C$ dates using 'BayLum'. We did not have OSL samples from AH III; thus the OSL ages start from sublayers IIIa, IIIb and IIIc, which resulted in 37–39 ka (68% CI) following 40–41 ka and 40–42 ka corresponding to the sublayers AH IV and AH IVa. Combining the OSL ages with $^{14}C$ dates resulted in 35–42 ka for AH III to AH IV (and sublayer IVa). Afterwards, the Middle Paleolithic ages started from sample GB6 with the age of 45–48 ka, continuing to the oldest sample of the sequence GB14 with the age of 75–81 ka. The convergence of the Markov chain Monte Carlo (MCMC) along with the age probability density are plotted for sample GB4 in SOM Figure S8 as an example. The Bayesian process converged after 4,000,000 iterations.

## 4. Discussion

### *4.1. Reliability of luminescence ages*

The OSL age results derived from the quartz grains are in good agreement with the $pIRIR_{290}$ ages from the polymineral fractions. The only exception was observed for sample GB8, for which the average of the confidence interval of the $pIRIR_{290}$ represents an age ca. 10% older than for quartz. A residual dose (hard bleachable signal) might be a reason for the older age of the polymineral compared to the quartz age. The measured residual doses for two samples of GB1 and GB14 were less than 4 Gy and, hence, not significant in comparison with the equivalent doses of 68 Gy and 124 Gy. However, there is no indication that laboratory bleaching is equivalent to the natural bleaching before sediment deposition. The residual doses obtained in our study agree with values published in Buylaert et al. (2012) considering well-bleached samples. The excellent agreement between the quartz ages in comparison with the corresponding polymineral ages suggests that the quartz and potassium feldspar grains in the polymineral were sufficiently bleached (Murray et al., 2012).

509 The probable critical point regarding the blue-OSL ages might be the poor recycling ratio (up to
510 13–18% lower than unity). These values are lower than what is usually accepted (within 10% of
511 unity) as a standard criterion (Wintle and Murray, 2006). However, here the good match between
512 blue-OSL ages with $pIRIR_{290}$ ages (on top of a good agreement with $^{14}C$ results) gives confidence on
513 the accuracy of these ages.

514 To see the dependency of estimated $D_e$ on the recycling ratio, additionally, we categorized the $D_e$
515 distribution of each sample (for six randomly selected samples, GB1, GB3, GB5, GB8, GB10, GB14)
516 based on their recycling ratios into two groups: group 1 with recycling ratios less than its average
517 alongside group 2 with recycling ratios larger than its average. The results listed in SOM Table S6,
518 indicate no difference between the $D_e$ of group I and 2 is observed for samples GB5 and GB8. The
519 discrepancies between the $D_e$ of two groups corresponding to GB10 and GB14 are negligible. Yet, the
520 observed $D_e$ differences from samples GB1 and GB3 are more noticeable compared to the other
521 samples; however, within uncertainties, they agree with one another. More importantly, the $D_e$s
522 calculated from both groups for GB1 and GB3 show no correlation between low or high recycling
523 ratio and the smaller or larger $D_e$. We, therefore, conclude that for our samples, neither low nor high
524 recycling ratio result in significant $D_e$ underestimation or overestimation.

525 Besides, it appears that the $^{14}C$ ages published in Baines et al. (2014) agree more with the OSL
526 ages in comparison with the two ages published in Becerra-Valdivia et al. (2017). These $^{14}C$ ages
527 increase gradually with depth and provide the same pattern as for the OSL ages. For layer III (the
528 first layer in the plot) it appears that the age of Baines et al. (2014; calibrated from Ghasidian et al.,
529 2019) is more consistent with the luminescence ages and it is likely that the $^{14}C$ age of layer III
530 (Becerra-Valdivia et al., 2017) is slightly older. Besides, the age of IVa (Becerra-Valdivia et al., 2017)
531 appears to be younger in comparison with luminescence ages. Finally, the good match of the two
532 distinctly obtained series of luminescence ages (quartz and polymineral), and the consistency of the
533 OSL ages with the $^{14}C$ ages provide reasonable confidence in the chronology for the top of the
534 sequence. For ages in the lower profile, OSL and $pIRIR_{290}$ ages agree with each other and are
535 stratigraphically consistent.

536

537 *4.2. The Bayesian approach toward more precise ages*

538 In Section 3.5, we combined the OSL ages with the available $^{14}C$ ages (Conard and Ghasidian,
539 2011; Baines et al., 2014; Becerra-Valdivia et al., 2017) to build up the Bayesian chronology using the
540 R package 'BayLum'. The correlation between OSL samples due to shared systematic error from the
541 instruments was addressed by creating a theta matrix. For all OSL dating measurements (both the
542 equivalent dose and the dose rate), the same instruments were employed except for the in situ
543 gamma-dose rate. We noticed that the gamma-dose rate of samples GB10 and GB11 (0.43 ± 0.02
544 and 0.39 ± 0.01 Gy $ka^{-1}$, respectively) deduced from laboratory measurements agreed with the in situ
545 gamma-dose rate of sample GB9 (0.40 ± 0.03 Gy $ka^{-1}$), which is in close location to samples GB10 and
546 GB11 in the profile with in situ gamma dose rate available (Fig. 2). Therefore, for these two samples,
547 we have employed the in situ gamma-dose rate of sample GB9. We have provided one theta matrix
548 considering (1) the uncertainties of in situ gamma-dose rates for samples GB1 to GB11, and (2) the
549 uncertainties of gamma-ray spectrometry for samples GB13 and GB14. We did not employ the in situ
550 gamma-dose rate of sample GB9 for samples GB13 and GB14 at the bottom since the environmental
551 situation is completely different with the rest of samples due to presence of a large rock in AH VI and
552 being close to the bedrock (Fig. 2).

553 Comparing Bayesian chronology in Figure 7 with the classical quartz ages in Figure 6 shows that
554 the Bayesian age intervals were considerably reduced, especially for the top of the sequence where
555 $^{14}C$ ages are available. To better illustrate the improvement of the uncertainty in the Bayesian
556 chronology, in Figure 8 we show classical quartz ages from Section 3.3 and the Bayesian quartz ages
557 (Section 3.5). The credible intervals created by the Bayesian approach are considerably smaller than
558 those confidence intervals of the classical approach. These reductions are significant (from 57% to a
559 maximum of 73%) where $^{14}C$ ages are combined with the OSL ages (from GB1 to GB4). Our results
560 show that combining OSL ages with $^{14}C$ ages in the Bayesian modeling when stratigraphic constraints
561 were also included indeed result in more precise chronologies. However, for GB6 to GB14, where no

562 $^{14}$C ages were available, Bayesian modeling provides more precise ages by reducing the uncertainties
563 (from 17% to a maximum of 40%). Heydari et al. (2020) observed similar improvements in the
564 precision of the Bayesian chronology caused by stratigraphic ordering even where only OSL ages are
565 involved. In that study, the authors emphasized the effect of applied stratigraphic constraints
566 leading to a reduction of overall uncertainty where samples' age intervals overlap one another. In
567 our study, the stratigraphic order also plays a role, in particular for sample GB1 to GB4, where their
568 age intervals overlap. However, the other reason for the uncertainty reduction is the inclusion of the
569 $^{14}$C ages as independent ages, since such combination, corrects the effect of systematic errors in OSL
570 dating and resulted in ages that are more precise.

571 Moreover, the result of the Bayesian chronology ended up with ages sometimes younger (like
572 GB2 and GB9) and sometimes older (GB7, GB10 and GB11) than the corresponding ages produced by
573 the classical approach of data analysis to satisfy the stratigraphic constraints. Besides, applying
574 stratigraphic constraints for samples GB13 and GB14, which belong to one layer, results in a younger
575 age for sample GB13 and older age for GB14. On the other hand, the classical ages show that the age
576 of GB14 is slightly younger than GB13. As a result, it can be concluded that applying stratigraphic
577 ordering might lead to underestimated or overestimated ages when age intervals overlap. Here we
578 believe that this discrepancy is not critical since the Bayesian ages overlap and they statistically are
579 not distinguishable.

580

581 *4.3. The obtained chronology in its Paleolithic context*

582 Ghār-e Boof is mainly recognized for its rich Upper Paleolithic assemblages based on bladelet
583 production named Rostamian tradition (Conard and Ghasidian, 2011, Ghasidian, 2014; Ghasidian et
584 al., 2017). The richest horizon linked to the Rostamin tradition is AH III. The Bayesian OSL results for
585 sublayers IIIa, IIIb and IIIc suggest that the producers of Rostamian tradition likely occupied the site
586 of Ghār-e Boof between 37–39 ka (68% CI). The obtain Bayesian chronology using both OSL ages and
587 $^{14}$ C dates resulted in 35–42 ka for AH III to AH IV (also sublayer IVa). Moreover, the result of

Bayesian modeling only for $^{14}C$ published in Becerra-Valdivia et al. (2017) yielded the age of 41,950–39,850 cal BP (in 68% CI), which corresponds to the beginnings of the Upper Paleolithic period for the site and for the Zagros as a whole. These results agree with the Bayesian OSL ages of the AH IV and AH IVa of 40–42 ka.

Sublayers AH IVc and AH IVd have low find densities and cannot at present be attributed with confidence to either the Middle or the Upper Paleolithic. Although Arjeneh point and perforated shells were observed in AH IV to AH IVb, which we attribute to the Upper Paleolithic, they are missing in AH IVc and AH IVd. As a result, the age of AH IVd 45–48 ka may be considered to represent the period between Middle Paleolithic and the Rostamian at Ghār-e Boof.

In summary, the Bayesian OSL ages determined for the Upper Paleolithic sequence of the site from AH IIIa to AH IVa resulted in ages of 37–42 ka (68% CI). This range agrees with the chronology for the Upper Paleolithic of the Shanidar cave in the north of Zagros which is in ca. 29–40 cal ka BP (original data: Solecki 1963; Hole and Flannery, 1968; recalculated data: Becerra-Valdivia et al., 2017). This result is also in agreement with the Upper Paleolithic chronology provided for the site of Yafteh associated with the Baradostian culture (Otte et al., 2011; ca. 29–42 cal ka BP). Aside from the controversial ages for the early Upper Paleolithic of the Kaldar cave with the range of ca. 37–54 cal ka BP (Bazgir et al., 2017), the results from Ghār-e Boof are consistent with the Upper Paleolithic chronology known elsewhere in the Zagros.

In general, the chronology for the Upper Paleolithic part of the site of Ghār-e Boof, like other sites mentioned in the Zagros Mountains, seems to be older than the chronology provided for the Paleolithic sites located in the north of central Iranian desert. For instance, the site of Garm roud 2, which is situated in the north of the Alborz Mountains region, suggests an Upper Paleolithic settlement between 28–35 cal ka BP (Berillon et al., 2007; Antoine et al., 2016). Moreover, the Bayesian OSL dating for the Upper Paleolithic sequence of the open-air site of Mirak (Vahdati Nasab et al., 2019) resulted in 21–28 ka (Heydari et al., 2020).

The Middle Paleolithic Bayesian OSL chronology from AH V starts with the age of 46–49 ka. Below, AH Va in the western and the northern wall the Bayesian ages result in 51–55 ka and 55–58 ka. The age results for the sublayers of AH V, AH Vb and AH Vc encompass the range of 56–60 ka and 58–63 ka. The two Bayesian ages for the last layer AH VI from the top and the bottom exhibited 72–78 ka and 75–81 ka. In summary, the chronology of the archaeological layers containing Middle Paleolithic assemblages shows a wide range of 45–81 ka, starting with the range of 72–81 ka and continuing to the very late Middle Paleolithic ca. 45 ka. The Middle Paleolithic deposits at Ghār-e Boof (AH IVd - AH VI) are not as rich as the Rostamian part of the sequence. Although the Middle Paleolithic assemblages have not yet been published in detail, we argue that there is no continuity is observed between the Middle Paleolithic and the bladelet assemblages of the Upper Paleolithic at Ghār-e Boof (Bretkze and Conard 2017; Conard and Zeidi 2019). The much lower density of the Middle Paleolithic assemblages appears to reflect sporadic, short-term occupations characterized by diverse scrapers and a dominance of flake production. These assemblages stand in stark contrast to the rich unidirectional bladelet production during the Rostamian. Also the rich record of personal ornaments, including numerous perforated shells and a perforated incisor of an ungulate (Conard and Ghasidian, 2011; Conard and Zeidi, 2019), is thus far limited to the Rostamian deposits. We hypothesize that the Rostamian appeared due to the presence of a new group of AMH in the region. This population was likely different from the humans who created the relatively sparse Middle Paleolithic record from period preceding the Rostamian. For the moment, we do not know which human species were responsible for Middle Paleolithic assemblages recovered from Ghār-e Boof. This being said, to date, the evidence available from sites in the Zagros including Bisitun Cave, Shanidar and Wezmeh suggest that Neanderthals were often responsible for making Middle Paleolithic assemblages (Coon, 1951; Solecki, 1963; Trinkaus, 1983; Zanolli et al., 2019). On the other hand, the complex record of human fossils dating to the Late Middle Pleistocene and Upper Pleistocene in southwestern Asia as a whole points to a long history of early modern humans in the macro-region and warns against rushing to hasty conclusions in the absence of human skeletal remains (Hershkovitz et al., 2018).

In summary, our study shows that Ghār-e Boof was occupied intensely during MIS (Marine Isotope Stage) 3 (after Lisiecki and Raymo, 2005) near the beginning of the Upper Paleolithic. The site was occupied during MIS 3, MIS 4 and MIS 5a by the makers of the Middle Paleolithic assemblages. Although many questions remain open, it is worth mentioning that the new Middle Paleolithic chronology for the site of Ghār-e Boof represents the first reliable absolute chronology for the Middle Paleolithic of the southern Zagros. Due to the unique location of Ghār-e Boof, and the likely association of the Rostamian with modern humans, our chronology provides insights into dispersal routes of early modern humans from Africa toward central Asia through the south of the Iranian Plateau. To decipher the full picture in the southern Zagros, more archaeological fieldwork and paleochronological studies are needed in the future.

## 5. Conclusions

We have presented a luminescence chronology based on quartz and the polymineral for the Middle and Upper sequences of the site of Ghār-e Boof. Our investigation showed that the $pIRIR_{290}$ ages for the polymineral fractions are in good agreement with the blue-OSL ages of the quartz grains. Additionally, previously published $^{14}C$ ages for the Upper Paleolithic part of the cave agree with the luminescence ages. We then applied Bayesian modeling, specifically designed for luminescence dating on blue-OSL quartz signals using the R package 'BayLum', which enabled us to incorporate the published $^{14}C$ ages and well-established stratigraphic constraints to further improve the precision of the chronology. The obtained Bayesian ages resulted in a significant improvement of precision by reducing the age uncertainties. The Bayesian ages of the Upper Paleolithic sequence of the cave for AH IIIa to IVa produced ages of 37–42 ka (68% CI). This result is in agreement with the chronology based on $^{14}C$ (Conard and Ghasidian 2011; Baines et al., 2014; Becerra-Valdivia et al., 2017).

664 The chronology obtained for the Middle Paleolithic sequence of the cave in AH IVd and AH VI
665 resulted in a wide age range of 45–81 ka (68% CI). This work provides a solid luminescence-based
666 chronology for the Middle Paleolithic period in Iran. Moreover, the Bayesian OSL chronology for the
667 site of Ghār-e Boof is the first complete luminescence dating of the Middle and the Upper Paleolithic
668 periods in the Zagros Mountain region in Iran. The radical change in material culture between the
669 Middle Paleolithic and Rostamian Upper Paleolithic occupations at Ghār-e Boof almost certainly
670 documents the occupation of the site by different groups of humans during MIS 3, MIS 4 and MIS 5a.
671 While we have good reasons to hypothesize that the Rostamian assemblages were left by AMH,
672 both Neanderthals and modern humans remain plausible candidates as the makers of the sites
673 Middle Paleolithic assemblages. Regardless of the specific identity of these populations, the
674 chronostratigraphic sequence from Ghār-e Boof points to a shift between the Middle Paleolithic and
675 Rostamian demographic groups within three millennia.

676

677 ## References

678 Aitken, M.J., 1985. Thermoluminescence Dating. Academic Press, London.

679 Antoine, P., Bahain, J.-J., Ghaleb, B., Mercier, N. 2016. The chronostratigraphic framework at Garm
680 Roud. In: Berillon, G., Asgari Khaneghah, A. (Eds.), Garm Roud: A Hunting Place in Iran, Upper
681 Paleolithic. Editions IFRI & @rchéo-éditions, Tehran, pp. 49-55 (in French-English-Persian).

682 Bailey, R.M., Smith, B.W., Rhodes, E.J., 1997. Partial bleaching and the decay from characteristics of
683 quartz OSL. Radiation Measurements 27, 123–136.

684 Bar-Yosef, O., Meignen, L., 2001. The chronology of the levantine Middle Palaeolithic period in
685 retrospect. Bulletins et Mémoires de la Société d'Anthropologie de Paris 13, 269-289.

686 Baines, J.A., Riehl, S., Conard, N.J., Zeidi-Kulehparcheh, M., 2014. Upper Palaeolithic archaeobotany
687 of Ghar-e Boof cave, Iran: a case study in site disturbance and methodology. Archaeological and
688 Anthropological Sciences 7, 245-256.

689 Bazgir, B., Ollé, A., Tumung, L., Becerra-Valdivia, L., Douka, K., Higham, T., van derMade, J., Picin, A.,
690 Saladié, P., López-García, J.M., Blain, H.A., Allué , E., Fernández-García , M., Rey-Rodríguez, I.,
691 Arceredillo, D., Bahrololoumi, F., Azimi, M.,Otte, M., Carbonell, E., 2017. Understanding the
692 emergence of modern humans and the disappearance of Neanderthals: Insights from Kaldar Cave
693 (Khorramabad Valley, Western Iran). Scientific Reports 7, 43460.
694 Becerra-Valdivia, L., Douka, K., Comeskey, D., Bazgir, B., Conard, N.J., Marean, C.W., Ollé , A., Otte,
695 M., Tumung, L., Zeidi, M., Higham, T.F.G., 2017. Chronometric investigations of the Middle to
696 Upper Paleolithic transition in the Zagros Mountains using AMS radiocarbon dating and Bayesian
697 age modelling. Journal of Human Evolution 109, 57-69.
698 Berillon, G., Khaneghah, A.A., Antoine, P., Bahain, J.-J., Chevrier, B., Zeitoun, V., Aminzadeh, N.,
699 Beheshti, M., Chanzanagh, H.E., Nochadi, S., 2007. Discovery of new open-air Paleolithic localities
700 in Central Alborz, Northern Iran. Journal of Human Evolution 52, 380–387.
701 Biglari, F., 2001. Recent finds of Paleolithic period from Bisotun, Central Western Zagros Mountains.
702 Iranian Journal of Archaeology and History 28, 50–60 (in Persian).
703 Bobek, H. 1968. Vegetation. In: Fisher, W.B. (Ed.), The Cambridge History of Iran, Vol. 1: The Land of
704 Iran. Cambridge University Press, Cambridge pp. 280-293.
705 Bos, A.J.J., Wallinga, J., 2012. How to visualize quartz OSL signal components. Radiation
706 Measurements 47, 752-758.
707 Boivin, N., Fuller, D.Q., Dennell, R., Allaby, R., Petraglia, M.D., 2013. Human dispersal across diverse
708 environments of Asia during the Upper Pleistocene. Quaternary International 300, 32–47.
709 Bretzke, K., Conard, N. J., 2017. Not just a crossroad: population dynamics and changing material
710 culture in southwestern Asia during the late Pleistocene. Current Anthropology 58 (Supplement
711 17), S449-S462.
712 Brooks, I. A., 1989. The Physical Geography, Geomorphology and Late Quaternary History of
713 Mahidasht Project Area, Qara Su Basin Central West Iran, ROM Mahidasht Project, Vol. 1. Royal
714 Ontario Museum, Toronto.

715 Buylaert, J.-P., Jain, M., Murray, A.S., Thomsen, K.J., Thiel, C., Sohbati, R., 2012. A robust feldspar
716 luminescence dating method for Middle and Late Pleistocene sediments. Boreas 41, 435-451.
717 Christoph, C., Philippe, A., Kreutzer, S., Guérin, G., 2019. 'BayLum': chronological Bayesian models
718 integrating optically stimulated luminescence and radiocarbon age dating. Version 0.1.4,
719 http://github.com/crp2a/BayLum.
720 Colarossi, D., Duller, G.A.T., Roberts, H.M., 2017. Exploring the behaviour of luminescence signals
721 from feldspars: Implications for the single aliquot regenerative dose protocol. Radiation
722 Measurements 109, 35-44.
723 Combès, B., Philippe, A., Lanos, P., Mercier, N., Tribolo, C., Guérin, G., Guibert, P., Lahaye, C., 2015. A
724 Bayesian central equivalent dose model for optically stimulated luminescence dating. Quaternary
725 Geochronology 28, 62–70.
726 Combès, B., Philippe, A., 2017. Bayesian analysis of individual and systematic multiplicative errors for
727 estimating ages with stratigraphic constraints in optically stimulated luminescence dating.
728 Quaternary Geochronology 39, 24–34.
729 Conard, N.J., Ghasidian, E., 2011. The Rostamian cultural group and thetaxonomy of the Iranian
730 Upper Paleolithic. In: Conard, N.J., Drechsler, P., Morales, A. (Eds.), Between Sand and Sea, The
731 Archaeology and Human Ecology of Southwestern Asia. Kerns Verlag, Tübingen, pp. 33–52.
732 Conard, N.J., Zeidi, M., 2019. New research on the Paleolithic occupation of Ghar-e Boof, Fars
733 Province. Archaeology: Journal of the Iranian Center for Archaeological Research 2, 7-16.
734 Conard, N.J., Ghasidian, E., Heydari-Guran, S., 2013. The Paleolithic of Iran. In The Oxford Handbook
735 of Ancient Iran. Potts, D.T. (Ed.), Oxford University Press, Oxford. pp. 29-48.
736 Coon, C.S., 1951. Cave Explorations in Iran 1949. University of Pennsylvania, Philadelphia.
737 Dietze, M., Kreutzer, S., Burow, C., Fuchs, M.C., Fischer, M., Schmidt, C., 2016. The abanico plot:
738 visualising chronometric data with individual standard errors. Quaternary Geochronology 31, 12–
739 18.
740 Duller, G.A.T., 2015. The Analyst software package for luminescence data: overview and recent
741 improvements. Ancient TL 33, 35–42.

742 Duller, G.A.T., 2003. Distinguishing quartz and feldspar in single grain luminescence measurements.
743 Radiation Measurements 37, 161–165.
744 Durcan, J.A., King, G., Duller, Geoff A.T., 2015. DRAC: dose rate and age calculator for trapped charge
745 dating. Quaternary Geochronology 28, 54–61.
746 Frayret, J., Castetbon, A., Trouve, G., Potin-Gautier, M., 2006. Solubility of (NH4)2SiF6, K2SiF6 and
747 Na2SiF6 in acidic solutions. Chemical Physics Letters 427, 356–364.
748 Frouin, M., Huot, S., Kreutzer, S., Lahaye, C., Lamothe, M., Philippe, A., Mercier, N., 2017. An
749 improved radiofluorescence single-aliquot regenerative dose protocol for Kfeldspars. Quaternary
750 Geochronology 38, 13–24.
751 Galbraith, R.F., Roberts, R.G., Laslett, G.M., Yoshida, H., Olley, J.M., 1999. Optical dating of single and
752 multiple grains of quartz from Jinmium rock shelter, northern Australia: Part I, experimental
753 design and statistical models. Archaeometry 41, 339-364.
754 Ganji, M.H., 1968. Climate. In: Fisher, W.B. (Ed.), The Cambridge History of Iran, Vol. 1: The Land of
755 Iran. Cambridge University Press, Cambridge, pp. 212-249.
756 Ghasidian, E., 2014. Early Upper Palaeolithic Occupation at the Ghār-e Boof Cave, a Reconstruction
757 of Cultural Traditions in Southern Zagros Mountains of Iran. Kerns Verlag, Tubingen.
758 Ghasidian, E., Bretzke, K., Conard, N. J., 2017. Excavations at Ghar-e Boof in the Fars Province of Iran
759 and its bearing on models for the evolution of the Upper Palaeolithic in the Zagros Mountains.
760 Journal of Anthropological Archaeology 47, 33–49.
761 Ghasidian, E., Heydari-Guran, S., Mirazón Lahr, M., 2019. Upper Palaeolithic cultural diversity in the
762 Iranian Zagros Mountains and the expansion of modern humans into Eurasia. Journal of Human
763 Evolution 132, 101-118.
764 Guérin, G., Mercier, N., Adamiec, G., 2011. Dose-rate conversion factors: update. Ancient TL 29, 5–8.
765 Guérin, G., Mercier, N., 2012. Preliminary insight into dose deposition processes in sedimentary
766 media on a grain scale: Monte Carlo modelling of the effect of water on gamma dose-rates.
767 Radiation Measurements 47, 541-547.

768 Guérin, G., Mercier, N., Nathan, R., Adamiec, G., Lefrais, Y., 2012. On the use of the infinite matrix
769 assumption and associated concepts: a critical review. Radiation Measurements 47, 778-785.
770 Guérin, G., Combès, B., Lahaye, C., Thomsen, K.J., Tribolo, C., Urbanova, P., Guibert, P.,Mercier, N.,
771 Valladas, H., 2015. Testing the accuracy of a bayesian central-dose model for single-grain osl,
772 using known-age samples. Radiation Measurements 81, 62-70.
773 Guérin, G., Christophe, C., Philippe, A., Murray, A.S., Thomsen, K.J., Tribolo, C., Urbanova, P., Jain,
774 M., Guibert, P., Mercier, N., Kreutzer, S., Lahaye, C., 2017. Absorbed dose, equivalent dose,
775 measured dose rates, and implications for OSL age estimates: Introducing the Average Dose
776 Model. Quaternary Geochronology 41, 163-173.
777 Guibert, P., Schvoerer, M., 1991. TL-dating: Low background gamma spectrometry as a tool for the
778 determination of the annual dose. Nuclear Tracks and Radiation Measurements, 14, 155-161.
779 Guibert, P., Lahaye, C., Bechtel, F., 2009. The importance of U-series disequilibrium of sediments in
780 luminescence dating: a case study at the Roc de Marsal Cave (Dordogne, France). Radiation
781 Measurements 44, 223-231.
782 Grün, R., Stringer, C., McDermott, F., Nathan, R., Porat, N., Robertson, S., Taylor, L., Mortimer, G.,
783 Eggins, S., McCulloch, M., 2005. U-Series and ESR analyses of bones and teeth relating to the
784 human burials from Skhul. Journal of Human Evolution 49, 316–334
785 Hansen, V., Murray, A.S., Buylaert, J.-P., Yeo, E.-Y., Thomsen, K.J., 2015. A new irradiated quartz for
786 beta source calibration. Radiation Measurements 81, 123–127.
787 Hershkovitz, I., Weber, G.W., Quam, R., Duval, M., Grün, R., Kinsley, L., Ayalon, A., Bar-Matthews, M.
788 Valladas, H., Mercier, N., Arsuaga, J.L., Martinon-Torres, M., Bermúdez de Castro, J.M., Fornai, C.,
789 Martín-Frances, L., Sarig, R., May, H.,Krenn, V.A., Slon, V., Rodríguez, L., García, R., Lorenzo, C.,
790 Carretero, J.M., Frumkin, A., Shahack-Gross, R., Bar-Yosef Mayer, D.E., Cui, Y., Wu, X., Peled, N.,
791 Groman-Yaroslavski, I., Weissbrod, L., Yeshurun, R., Tsatskin, A., Zaidner, Y., Weinstein-Evron, M.,
792 2018. The earliest modern humans outside Africa. Science 359, 456-459.
793 Heydari, M., Guérin, G., 2018. OSL signal saturation and dose rate variability: Investigating the
794 behaviour of different statistical models. Radiation Measurements 120, 96–103.

795 Heydari, M., Guérin, G., Kreutzer, S., Jamet, G., Akhavan Kharazian, M., Hashemi, M., Vahdati Nasab,
796 H., Berillon, G., 2020. Do Bayesian methods lead to more precise chronologies? 'BayLum' and a
797 first OSL-based chronology for the Palaeolithic open-air site of Mirak (Iran). Quaternary
798 Geochronology 59, 101082.
799 Heydari-Guran, S., 2014. Paleolithic Landscapes of Iran. Archaeopress, Oxford.
800 Heydari-Guran, S., Ghasidian, E., 2017. The MUP Zagros Project: tracking the Middle-Upper
801 Palaeolithic transition in the Kermanshah region, west-central Zagros, Iran. Antiquity 91 (355), 1-
802 7.
803 Higham, T., 2011. European Middle and Upper Palaeolithic radiocarbon dates are often older than
804 they look: problems with previous dates and some remedies. Antiquity 85, 235–249.
805 Hole, F., Becerra Flannery, K.V., 1968. The prehistory of southwestern Iran: A preliminary report.
806 Proceedings of the Prehistoric Society 33, 147–206.
807 Huntley, D.J., Godfrey-Smith, D.I., Thewalt, M.L.W., 1985. Optical dating of sediments. Nature 313,
808 105–107.
809 Huntley, D.J., Baril, M.R., 1997. The K content of the K-feldspar being measured in optical dating or
810 in thermoluminescence dating. Ancient TL 15, 11–13.
811 Huntley, D.J., Lamothe, M., 2001. Ubiquity of anomalous fading in K-feldspar and the measurement
812 and correction for it in optical dating. Canadian Journal of Earth Sciences 38, 1093-1106.
813 Hütt, G., Jaek, I., and Tchonka, J. 1988. Optical dating: K-feldspars optical response stimulation
814 spectra. Quaternary Science Reviews 7, 381–385.
815 Jaubert, J., Biglari, F., Bordes, J.-G., Bruxelles, L., Mourre, V., Shidrang, S., Naderi, R.,Alipour, S., 2006.
816 New research on Paleolithic of Iran: preliminary report of 2004 Iranian-French joint mission.
817 Archaeological Reports 4, 17-26.
818 Krbetschek, M.R., Rieser, U., Zöller, L., Heinicke, J., 1994. Radioactive disequilibria in
819 palaeodosimetric dating of sediments. Radiation Measurements 23, 485–489.

820 Kreutzer, S., Martin, L., Guérin, G., Tribolo, C., Selva, P., Mercier, N., 2018. Environmental dose rate
821 determination using a passive dosimeter: Techniques and workflow for alpha-Al2O3:C chips.
822 Geochronometria 45, 56–67.
823 Li, B., Li, S.H., 2011. Luminescence dating of K-feldspar from sediments: a protocol without
824 anomalous fading correction. Quaternary Geochronology 6, 468-479.
825 Li, B., Li, S.H., 2012. A reply to the comments by Thomsen et al. on "Luminescence dating of K-
826 feldspar from sediments: A protocol without anomalous fading correction". Quaternary
827 Geochronology 8, 49-51.
828 Lisiecki, L.E., Raymo, M.E., 2005. A Pliocene-Pleistocene stack of 57 globally distributed benthic $\delta^{18}O$
829 records. Paleoceanography 20, 1–17.
830 Mauz ,B., Packman, S., Lang, A.2006. The alpha effectiveness in silt-sized quartz: New data obtained
831 by single and multiple aliquot protocols. Ancient TL 24, 47-52.
832 Mejdahl, V., 1987. Internal radioactivity in quartz and feldspar grains. Ancient TL 5, 10–17.
833 Mellars, P., 2006. Why did modern human populations disperse from Africa ca. 60,000 years ago? A
834 new model. Proceedings of the National Academy of Sciences USA 103, 9381-9386.
835 Meignen, L., 2012. Levantine perspectives on the Middle to Upper Paleolithic “transition”.
836 Archaeology, Ethnology and Anthropology of Eurasia 40(3), 12-21.
837 Millard, A., 2006. Bayesian analysis of ESR dates, with application to border cave. Quaternary
838 Geochronology 1, 159-166.
839 Motiei, H., 1993. Stratigraphy of Zagros. In: Treatise on the Geology of Iran. Iran Geological Survey,
840 Tehran, pp. 281-289 (in Farsi).
841 Murray, A.S., Wintle, A.G., 2000. Luminescence dating of quartz using an improved single-aliquot
842 regenerative-dose protocol. Radiation Measurements 32, 57–73.
843 Murray, A.S., Thomsen, K.J., Masuda, N., Buylaert, J.P., Jain, M., 2012. Identifying well-bleached
844 quartz using the different bleaching rates of quartz and feldspar luminescence signals. Radiation
845 Measurements 47, 688–695.

Nathan, R.P., Mauz, B., 2008. On the dose-rate estimate of carbonate-rich sediments for trapped charge dating. Radiation Measurements 43, 14-25.

Nishiaki, Y., Akazawa, T., 2018. Archeological issues in the Middle and Upper Paleolithic of the Levant and its neighboring regions. In: Nishiaki, Y., Akazawa, T. (Eds.), The Middle and Upper Paleolithic Archeology of the Levant and Beyond. Springer International Publishing, Singapore, pp. 133-156.

Otte, M., Shidrang, S., Zwyns, N., Flas, D., 2011. New radiocarbon dates for the Zagros Aurignacian from Yafteh cave, Iran. Journal of Human Evolution 61, 340–346.

Petraglia, M.D., Haslam, M., Fuller D.Q., Boivin, N., Clarkson, C., 2010. Out of Africa: new hypotheses and evidence for the dispersal of *Homo sapiens* along the Indian Ocean rim. Annals of Human Biology 37, 288–311.

Philippe, A., Guérin, G., Kreutzer, S., 2018. 'BayLum' an R package for Bayesian analysis of OSL ages: An introduction. Quaternary Geochronology 49, 16-24.

Prescott, J.R., Stephan, L.G., 1982. The contribution of cosmic radiation to the environmental dose for thermoluminescence dating. Latitude, altitude and depth dependences. Journal of European Study Group on Physical, Chemical, Biological and Mathematical Techniques Applied to Archaeology 6, 17-25.

Prescott, J.R., Hutton, J.T., 1994. Cosmic ray contributions to dose rates for luminescence and ESR dating: large depths and long-term time variations. Radiation Measurements 23, 497-500.

Preusser, F., Degering, D., Fuchs, M., Hilgers, A., Kadereit, A., Klasen, N., Krbetschek, M.R., Richter, D., Spencer, J.Q.G., 2008. Luminescence dating: basics, methods and applications. Eiszeitalter und Gegenwart 57, 95–149.

R Core Team, 2019. R: A language and environment for statistical computing. R Foundation for Statistical Computing, Vienna.

Richter, D., Richter, A., Dornich, K., 2013. lexsyg — a new system for luminescence research. Geochronometria 40, 220–228.

Richter, D., Richter, A., Dornich, K., 2015. Lexsyg smart — a luminescence detection system for dosimetry, material research and dating application. Geochronometria 42, 202–209.

873 Reimer, P.J., Bard, E., Bayliss, A., Beck, J.W., Blackwell, P.C., Bronk Ramsey, C., Buck, C.E., Cheng, H.,
874 Edwards, R.L., Friedrich, M., Grootes, P.M., Guilderson, T.P., Haflidason, H., Hajdas, I., Hatte, C.,
875 Heaton, T.J., Hoffmann, D.L., Hogg, A.G., Hughen, K.A., Kaiser, K.F., Kromer, B., Manning, S.W.,
876 Niu, M., Reimer, R.W., Richards, D.A., Scott, E.M., Southon, J.R., Staff, R.A., Turney, C.S.M., van
877 der Plicht, J., 2013. IntCal13 and Marine13 radiocarbon age calibration curves 0-50000 years cal
878 BP. Radiocarbon 55, 1869–1887.
879 Rhodes, E., Bronk Ramsey, C., Outram, Z., Batt, C., Willis, L., Dockrill, S., Bond, J., 2003. Bayesian
880 methods applied to the interpretation of multiple OSL dates: high precision sediment ages from
881 old scatness broch excavations, Shetland isles. Quaternary Science Reviews 22, 1231-1244.
882 Rosenberg, T.M., Preusser, F., Fleitmann, D., Schwalb, A., Penkman, K., Schmid, T.W., Al-Shanti,
883 M.A., Kadi, K., Matter, A., 2011. Humid periods in southern Arabia: Windows of opportunity for
884 modern human dispersal. Geology 39: 1115-1118.
885 Schmit, C., Bosken, J., Kolb, T., 2018. Is there a common alpha efficiency in polymineral samples
886 measured by various infrared stimulated luminescence protocols? Geochronometria 45, 160-172.
887 Shea JJ. 2003. The Middle Paleolithic of the East Mediterranean Levant. Journal of World Prehistory
888 17, 313–394.
889 Shea, J.J., 2010. Neanderthals and *Homo sapiens* in the Levant. In: Garcea, E.A.A. (Ed.), South-
890 Eastern Mediterranean Peoples Between 130,000 and 10,000 Years Ago. Oxbow Books, Oxford,
891 pp. 126-143.
892 Shidrang, S., Biglari, F., Bordes, J.-G., Jaubert, J., 2016. Continuity and change in the Late Pleistocene
893 lithic industries of the central Zagros: a typo-technological analysis of lithic assemblages from
894 Ghare-e Khar Cave, Bisotun, Iran. Archaeology Ethnology and Anthropology of Eurasia 44, 27-38.
895 Smedley, R.K., Duller, G.A.T., Pearce, N.J.G., Roberts, H.M., 2012. Determining the K-content of
896 single-grains of feldspar for luminescence dating. Radiation Measurements 47, 790-796.
897 Smith, P.E.L., 1986. Paleolithic Archaeology in Iran. The University Museum, University of
898 Pennsylvania, Philadelphia.
899 Solecki, R.S., 1963. Prehistory in Shanidar Valley, northern Iraq. Science 139, 179-193.

900 Solecki, R.S., Solecki, R.L., 1993. The pointed tools from the Mousterian occupations of Shanidar
901 Cave, northern Iraq. In: Olszewski, D., Dibble, H. (Eds.), The Paleolithic Prehistory of the Zagros-
902 Taurus. The University Museum of Archaeology and Anthropology, University of Pennsylvania,
903 Philadelphia, pp. 119-146.
904 Spooner, N.A., 1992. Optical dating: Preliminary results on the anomalous fading of luminescence
905 from feldspars. Quaternary Science Reviews 11, 139-145.
906 Stöcklin, J., Navabi, M.H., 1973. Tectonic Map of Iran. Iran Geological Survey, Tehran.
907 Thomsen, K.J., Murray, A.S., Jain, M., Botter-Jensen, L., 2008. Laboratory fading rates of various
908 luminescence signals from feldspar-rich sediment extracts. Radiation Measurements 43, 1474-
909 1486.
910 Thomsen, K.J., Murray, A.S., Jain, M., 2011. Stability of IRSL signals from sedimentary K-feldspar
911 samples. Geochronometria 38, 1–13.
912 Thiel, C., Buylaert, J.P., Murray, A.S., Terhost, B., Hofer, I., Tsukamoto, S., Frechen, M., 2011.
913 Luminescence dating of the Stratzing loess profile (Austria) – Testing the potential of an elevated
914 temperature post-IR IRSL protocol. Quaternary International 234, 23-31.
915 Trautmann, T., Krbetschek, M.R., Dietrich, A., Stolz, W., 1999. Feldspar radioluminescence: a new
916 dating method and its physical background. Journal of Luminescence 85, 45–58.
917 Trautmann, T., Krbetschek, M.R., Dietrich, A., Stolz, W., 1998. Investigations of feldspar
918 radioluminescence: potential for a new dating technique. Radiation Measurements 29, 421–425.
919 Trinkaus, E., 1983. The Shanidar Neandertals. Academic Press, New York.
920 Trinkaus, E., 2005. Early modern humans. Annual Review of Anthropology 34, 207-230.
921 Trinkaus, E., Biglari, F., Mashkour, M., Monchot, H., Reyss, J.L., Rougier, H., Heydari, S., Abdi, K.,
922 2008. Late Pleistocene human remains from Wezmeh Cave, Western Iran. American Journal of
923 Physical Anthropology 135, 371-378.
924 Tsanova, T., 2013. The beginning of the Upper Paleolithic in the Iranian Zagros. A taphonomic
925 approach and techno-economic comparison of Early Baradostian assemblages from Warwasi and
926 Yafteh (Iran). Journal of Human Evolution 65, 39-64.

927 Valladas, G., 1978. A gamma ray irradiator. Journal of European Study Group on Physical, Chemical,
928 Biological and Mathematical Techniques Applied to Archaeology 2, 439–442.
929 Vahdati Nasab, H., Clark., G.A., Torkamandi, S., 2013. Late Pleistocene dispersal corridors across the
930 Iranian plateau: A case study from Mirak, a Middle Paleolithic site on the northern edge of the
931 Iranian central desert (Dasht-e Kavir). Quaternary International 300, 267–281.
932 Vahdati Nasab,H., Berillon, G., Jamet, G., Hashemi, M., Jayez, M., Khaksar, S., Anvari, Z., Guérin, G.,
933 Heydari, M., Akhavan Kharazian,M., Puaud, S., Bonilauri, S., Zeitoun, V., Sévêque, N., Darvishi
934 Khatooni, J., Asgari Khaneghah A., 2019. The open-air Paleolithic site of Mirak, northern edge of
935 the Iranian Central Desert (Semnan, Iran): Evidence of repeated human occupations during the
936 late Pleistocene. Comptes Rendus Palevol 18, 465-478.
937 Vandenberghe, D., De Corte, F., Buylaert, J.P., Kučera, Van den haute, J.P., 2008. On the internal
938 radioactivity in quartz. Radiation Measurements 43, 771–775.
939 Wintle, A.G., 1973. Anomalous fading of thermoluminescence in mineral samples. Nature 245, 143–
940 144.
941 Wintle, A.G., Murray A.S., 2006. A review of quartz optically stimulated luminescence characteristics
942 and their relevance in single-aliquot regeneration dating protocols. Radiation Measurements 41,
943 369–391.
944 Zanolli, C., Biglari, F., Mashkour, M., Abdi, K., Monchot, H., Debue, K., Mazurier, A., Bayle, P., Luyer,
945 M., Rougier, H., Trinkaus, E., Macchiarelli, R., 2019. A Neanderthal from the Central Western
946 Zagros, Iran. Structural reassessment of the Wezmeh 1 maxillary premolar. Journal of Human
947 Evolution 135, 102643.
948 Zhang, J., Li, S.H., 2020. Review of the post-IR IRSL dating protocols of K-feldspar. Methods and
949 Protocols 3, 7.
950 Zeidi, M., Conard, N.J., 2019. Report on the fourth season of excavation at Ghār-e Boof in Rostam
951 County, Fars Province. In: Shirazi, R.A., (Ed.), 16th Annual Symposium of the Iranian Archaeology.
952 Iranian Center for Archaeological Research, Tehran, pp. 234-238 (in Farsi).

953

954

## Figure captions

**Figure 1.** a) Dasht-e Rostam region; the dashed areas show Dasht-e Rostam I and Dasht-e Rostam II, the site of Ghār-e Boof is located at the microhabitat of Yagheh Sangar. b) Location of the Paleolithic sites in the region, as mentioned in the text. c) Photo of the site of Ghār-e Boof.

**Figure 2.** Synthetic stratigraphic sections of the western and northern walls of the site of Ghār-e Boof. Locations of the luminescence samples, as well as the $^{14}C$ dates published in Conard and Ghasidian (2011), Baines et al. (2014) and Becerra-Valdivia et al. (2017) are shown.

**Figure 3.** TL curves, shine-down curves and typical dose-response curves of samples GB1 for both quartz (a) and polymineral fractions (b). Abbreviations: TL = thermoluminescence; OSL= optically stimulated luminescence; IRSL= infrared stimulated luminescence.

**Figure 4.** Distribution of equivalent doses of samples GB3 and GB14 as examples from the quartz (a, b) and polymineral fractions (c, d). The final equivalent doses are determined based on arithmetic average, and the uncertainty is estimated according to the standard error of the mean. Abbreviations: $D_e$ = equivalent dose; *n* = number of aliquots; abs. se = absolute standard error.

**Figure 5.** Radioactive disequilibrium check for the $^{238}U$ decay chain. The ratios of $^{238}U$ (post-$^{226}Ra$)/$^{232}Th$ and $^{238}U$ (pre-$^{226}Ra$)/$^{232}Th$ for the entire samples are shown. Most of the samples lie close to the equilibrium line except for samples GB2, GB4, GB7, GB10, GB13, and GB14 (they are color-coded in red). For these samples, averages of the top (pre-$^{226}Ra$) and the bottom (post-$^{226}Ra$) of the $^{238}U$ decay chain were used to determine the dose rates.

**Figure 6.** Results of the quartz OSL ages and $pIRIRSL_{290}$ ages of the polymineral fractions within 68 % confidence interval. The quartz and polymineral ages overlap one another, and they gradually

981 increase with depth. The $^{14}C$ ages (2014) are taken from Conard and Ghasidian (2011) and Baines et
982 al. (2014), while the $^{14}C$ ages (2017) are taken from Becerra-Valdivia et al. (2017). Abbreviations:
983 OSL= optically stimulated luminescence; $pIRIRSL_{290}$ = post-infrared infrared stimulated luminescence
984 at 290 °C.
985
986 **Figure 7.** Ages obtained after incorporating the Bayesian OSL (optically stimulated luminescence)
987 ages with the calibrated $^{14}C$ dates published in Conard and Ghasidian (2011), Baines et al. (2014),
988 and Becerra-Valdivia et al.(2017) using the R package 'BayLum'. The Bayesian model addresses the
989 shared systematic error between samples, and it also includes stratigraphic constraints.
990
991 **Figure 8.** Comparison of the OSL (optically stimulated luminescence) Bayesian quartz ages with the
992 ages derived from the classical approach. As illusterated applying stratigraphic constraints and
993 incorporating the $^{14}C$ dates play a fundamental role in reducing the uncertainties at the top of the
994 age sequence. However, even at the bottom where age intervals overlap with one another, the
995 Bayesian uncertainties are smaller than the corresponding classical approach.

51°12′E
51°24′E
51°36′E
30°36′N
30°24′N
30°12′N
a
Kohgiluyeh and Buyer Ahmad
Shiv
II
Fars
Ghar-e Boof
Baba Meydan
I
Zohreh
Fahliyan
Fahliyan
Heydari et al., 07/2020
0
5
10 km
45°E
60°E
36°N
24°N
b
Armenia
Azerbaijan
Turkmenistan
Shanidar
Gram Roud 2
Syria
Mirak
Iraq
Iran
Iran
Afghanistan
Yafteh
Ghar-e Boof
c
Elevation [m a.s.l.]
<= 0
250
500
1000
2000
3000
4000
DEM central map: ASTER GDEM 2 a product of METI and NASA.
Other data: Google Earth and Natural Earth @ naturalearthdata.com
Central map projection: WGS 84 / UTM Zone 39N
Mapping tool: QGIS 3.8.3
[map version: 2020-07-15]
Archaeological site
Province
City
Road
River/Seasonal stream
Floodplains
Valley plain

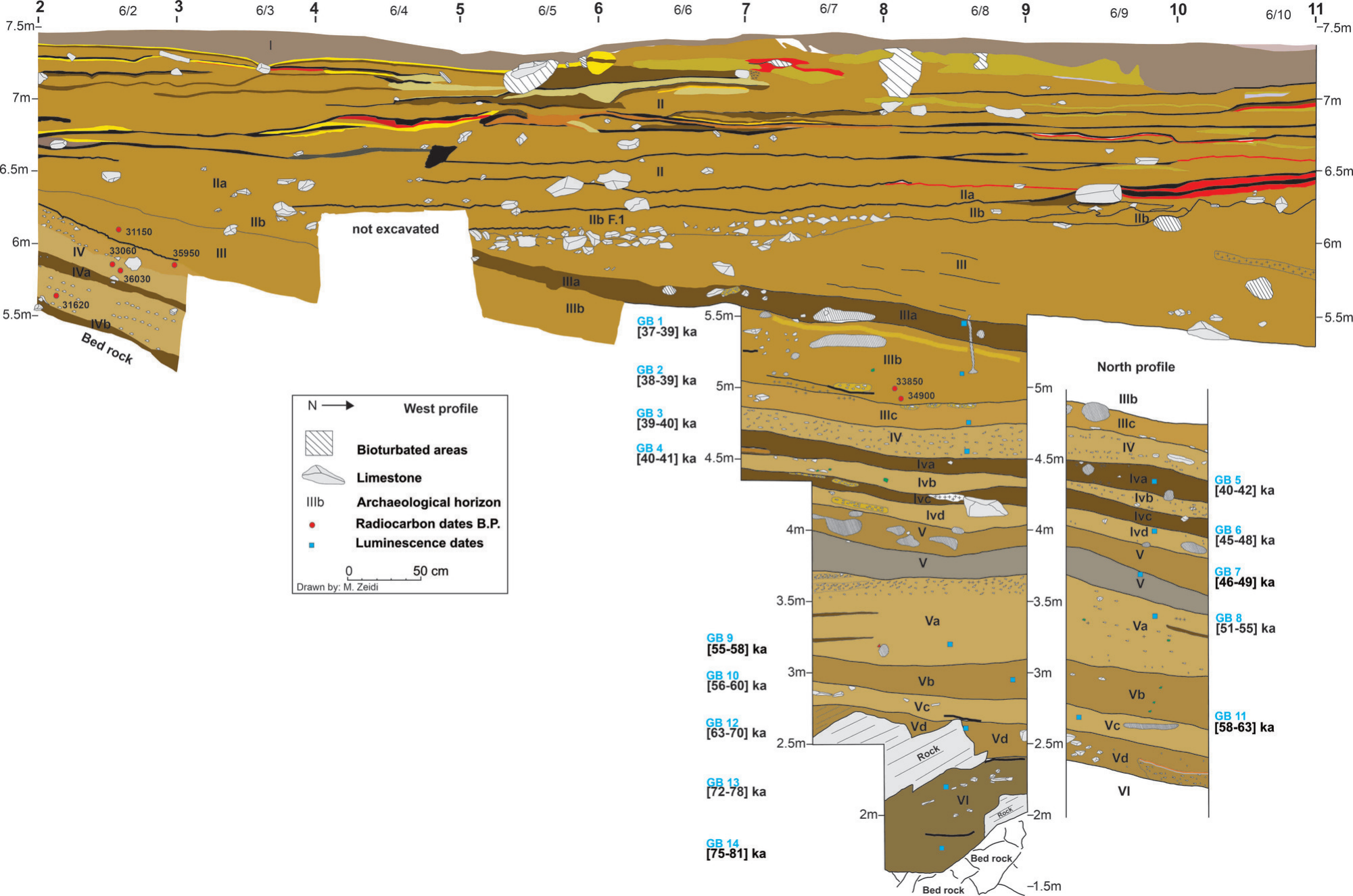
2
6/2
3
6/3
4
6/4
5
6/5
6
6/6
7
6/7
8
6/8
9
6/9
10
6/10
11
7.5m
7m
6.5m
6m
5.5m
5m
4.5m
4m
3.5m
3m
2.5m
2m
1.5m
I
II
IIa
IIb
IIb F.1
not excavated
III
IIIa
IIIb
IIIc
IV
IVa
IVb
IVc
IVd
V
Va
Vb
Vc
Vd
VI
31150
33060
35950
36030
31620
33850
34900
Bed rock
Rock
GB 1 [37-39] ka
GB 2 [38-39] ka
GB 3 [39-40] ka
GB 4 [40-41] ka
GB 5 [40-42] ka
GB 6 [45-48] ka
GB 7 [46-49] ka
GB 8 [51-55] ka
GB 9 [55-58] ka
GB 10 [56-60] ka
GB 11 [58-63] ka
GB 12 [63-70] ka
GB 13 [72-78] ka
GB 14 [75-81] ka
N
West profile
North profile
Bioturbated areas
Limestone
Archaeological horizon
Radiocarbon dates B.P.
Luminescence dates
0
50 cm
Drawn by: M. Zeidi

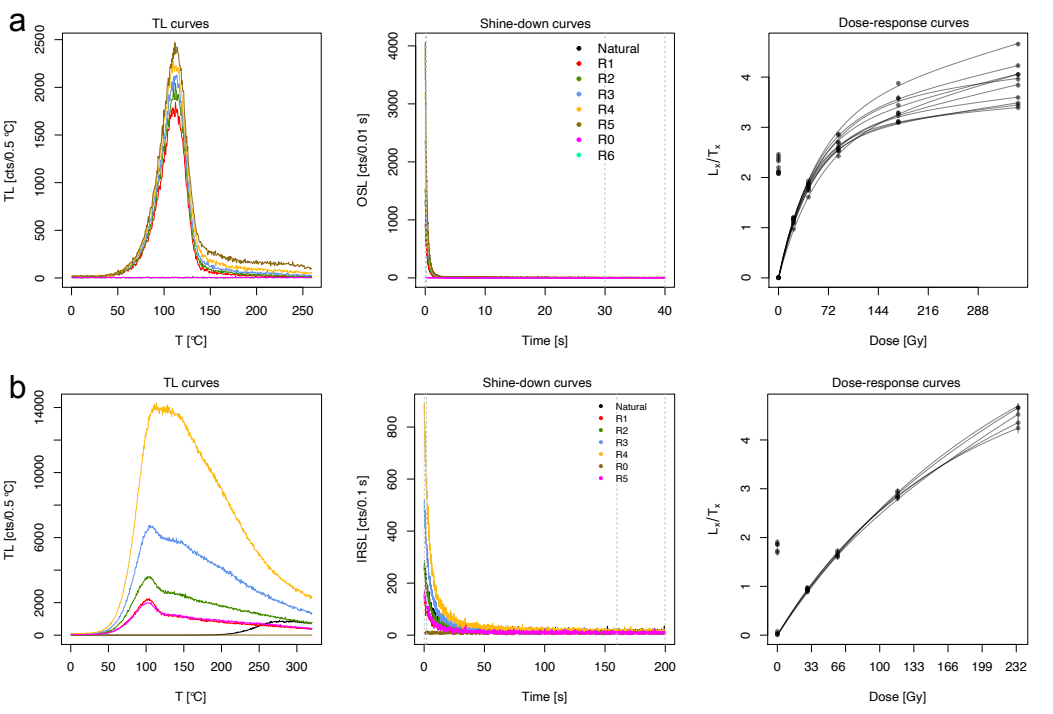
a
TL curves
TL [cts/0.5 °C]
T [°C]
Shine-down curves
OSL [cts/0.01 s]
Time [s]
Natural
R1
R2
R3
R4
R5
R0
R6
Dose-response curves
$L_x/T_x$
Dose [Gy]
b
TL curves
TL [cts/0.5 °C]
T [°C]
Shine-down curves
IRSL [cts/0.1 s]
Time [s]
Natural
R1
R2
R3
R4
R0
R5
Dose-response curves
$L_x/T_x$
Dose [Gy]

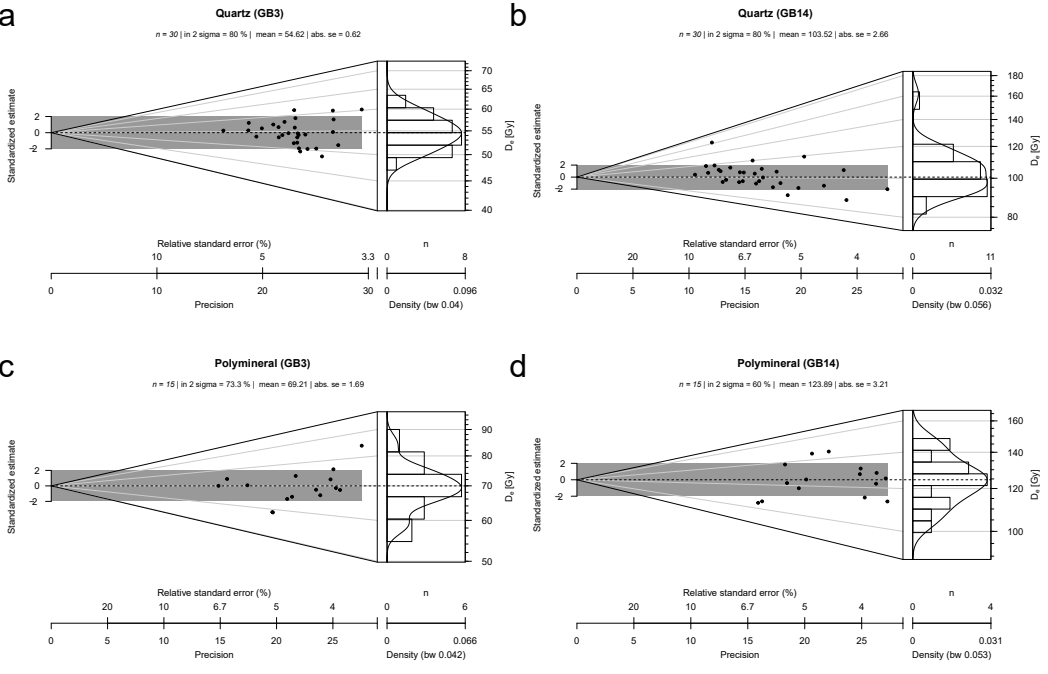
a
Quartz (GB3)
n = 30 | in 2 sigma = 80 % | mean = 54.62 | abs. se = 0.62
Standardized estimate
De [Gy]
Relative standard error (%)
n
Precision
Density (bw 0.04)
b
Quartz (GB14)
n = 30 | in 2 sigma = 80 % | mean = 103.52 | abs. se = 2.66
Standardized estimate
De [Gy]
Relative standard error (%)
n
Precision
Density (bw 0.056)
c
Polymineral (GB3)
n = 15 | in 2 sigma = 73.3 % | mean = 69.21 | abs. se = 1.69
Standardized estimate
De [Gy]
Relative standard error (%)
n
Precision
Density (bw 0.042)
d
Polymineral (GB14)
n = 15 | in 2 sigma = 60 % | mean = 123.89 | abs. se = 3.21
Standardized estimate
De [Gy]
Relative standard error (%)
n
Precision
Density (bw 0.053)

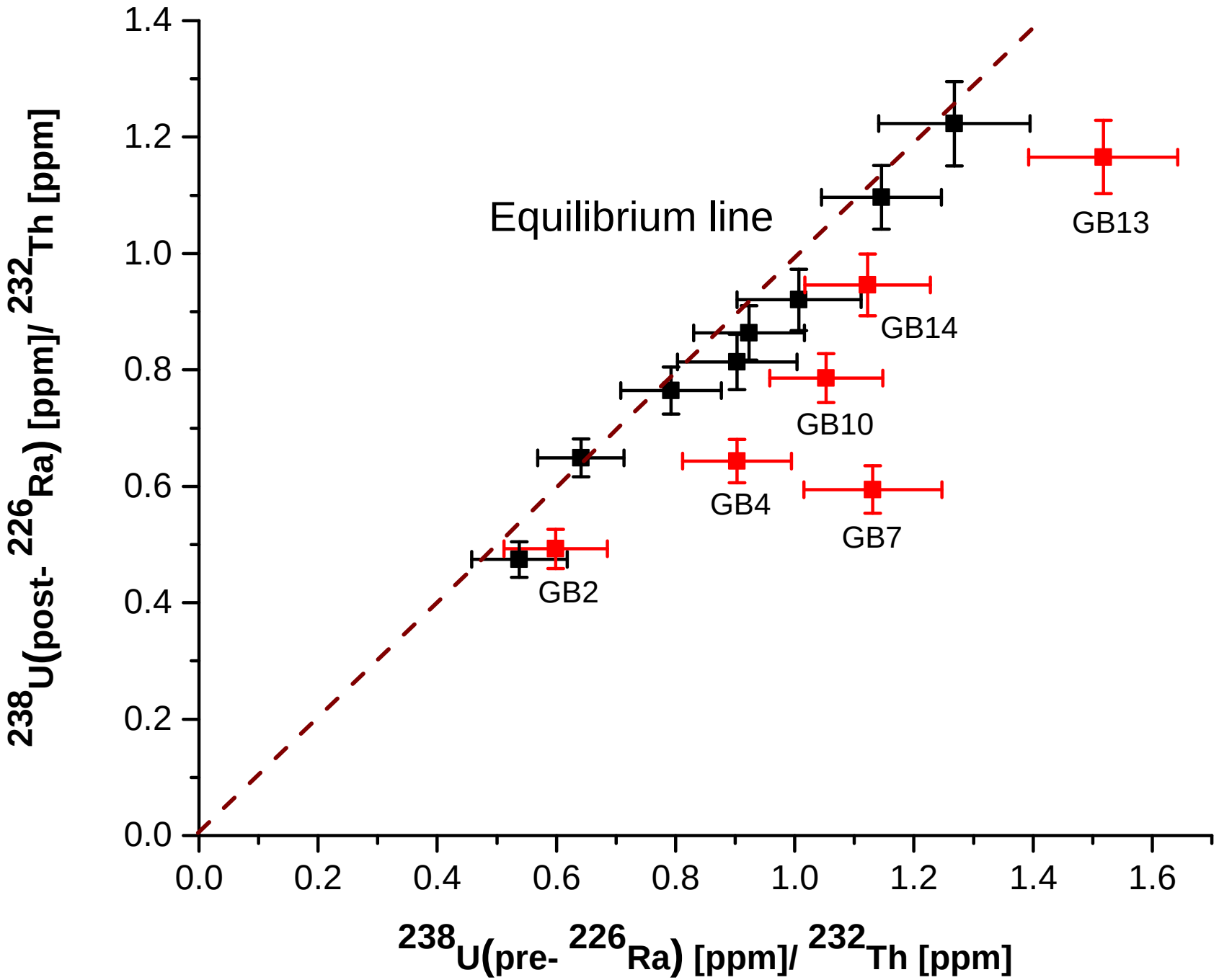
Equilibrium line
GB13
GB14
GB10
GB4
GB7
GB2
1.4
1.2
1.0
0.8
0.6
0.4
0.2
0.0
0.0
0.2
0.4
0.6
0.8
1.0
1.2
1.4
1.6
238U(post- 226Ra) [ppm]/ 232Th [ppm]
238U(pre- 226Ra) [ppm]/ 232Th [ppm]

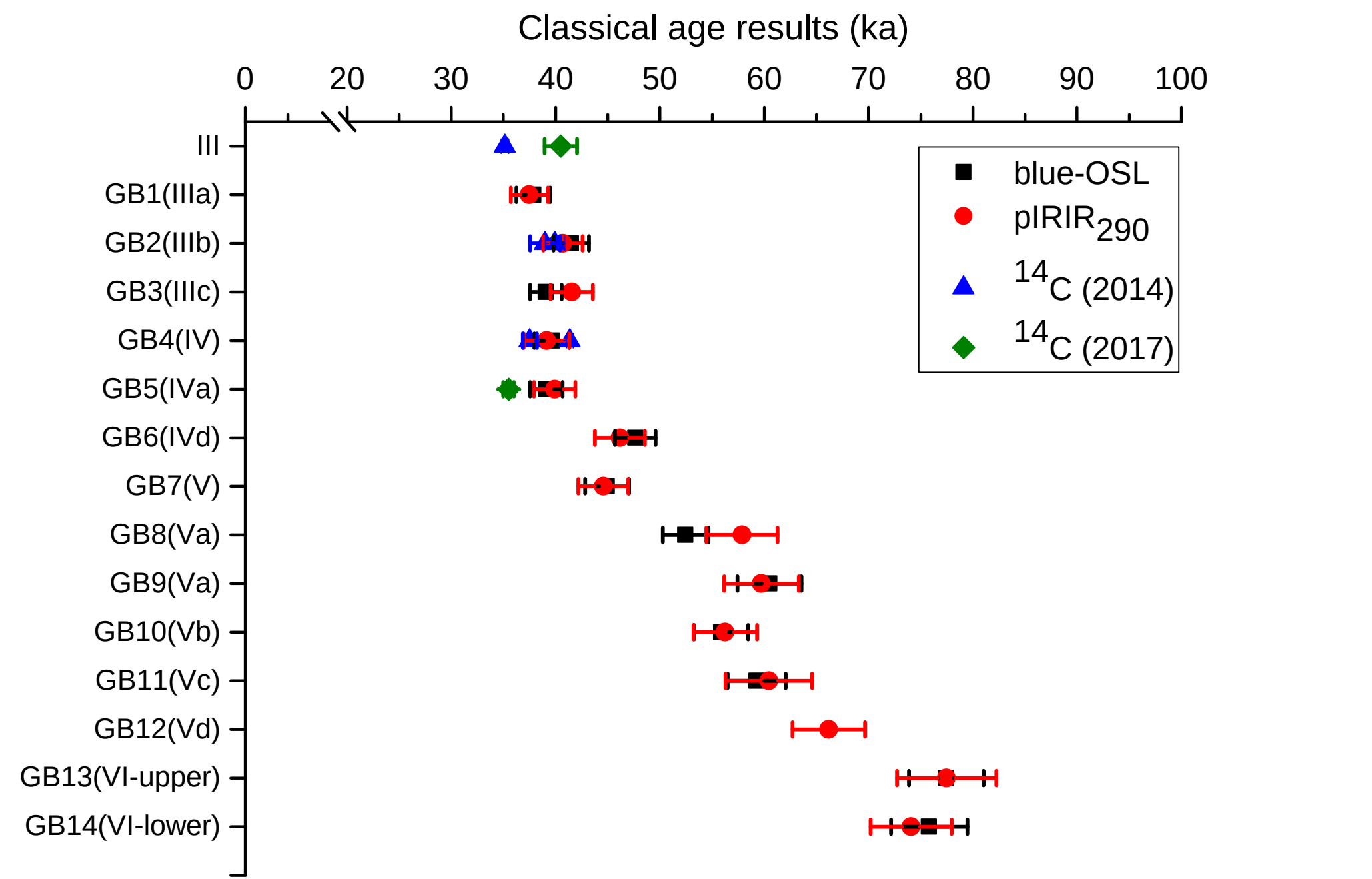
Classical age results (ka)
0
20
30
40
50
60
70
80
90
100
III
GB1(IIIa)
GB2(IIIb)
GB3(IIIc)
GB4(IV)
GB5(IVa)
GB6(IVd)
GB7(V)
GB8(Va)
GB9(Va)
GB10(Vb)
GB11(Vc)
GB12(Vd)
GB13(VI-upper)
GB14(VI-lower)
blue-OSL
pIRIR290
14C (2014)
14C (2017)

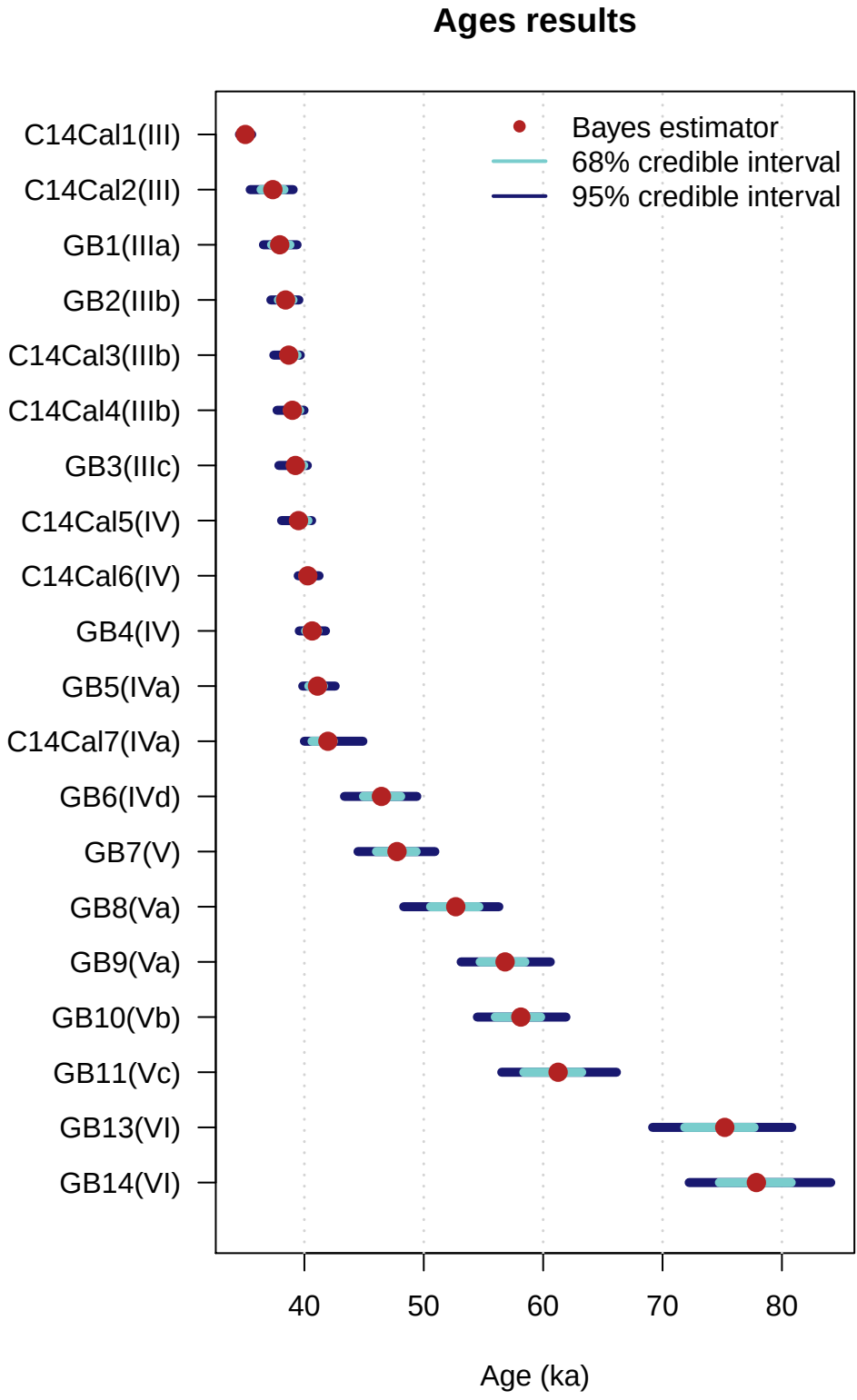
Ages results
Bayes estimator
68% credible interval
95% credible interval
C14Cal1(III)
C14Cal2(III)
GB1(IIIa)
GB2(IIIb)
C14Cal3(IIIb)
C14Cal4(IIIb)
GB3(IIIc)
C14Cal5(IV)
C14Cal6(IV)
GB4(IV)
GB5(IVa)
C14Cal7(IVa)
GB6(IVd)
GB7(V)
GB8(Va)
GB9(Va)
GB10(Vb)
GB11(Vc)
GB13(VI)
GB14(VI)
40
50
60
70
80
Age (ka)

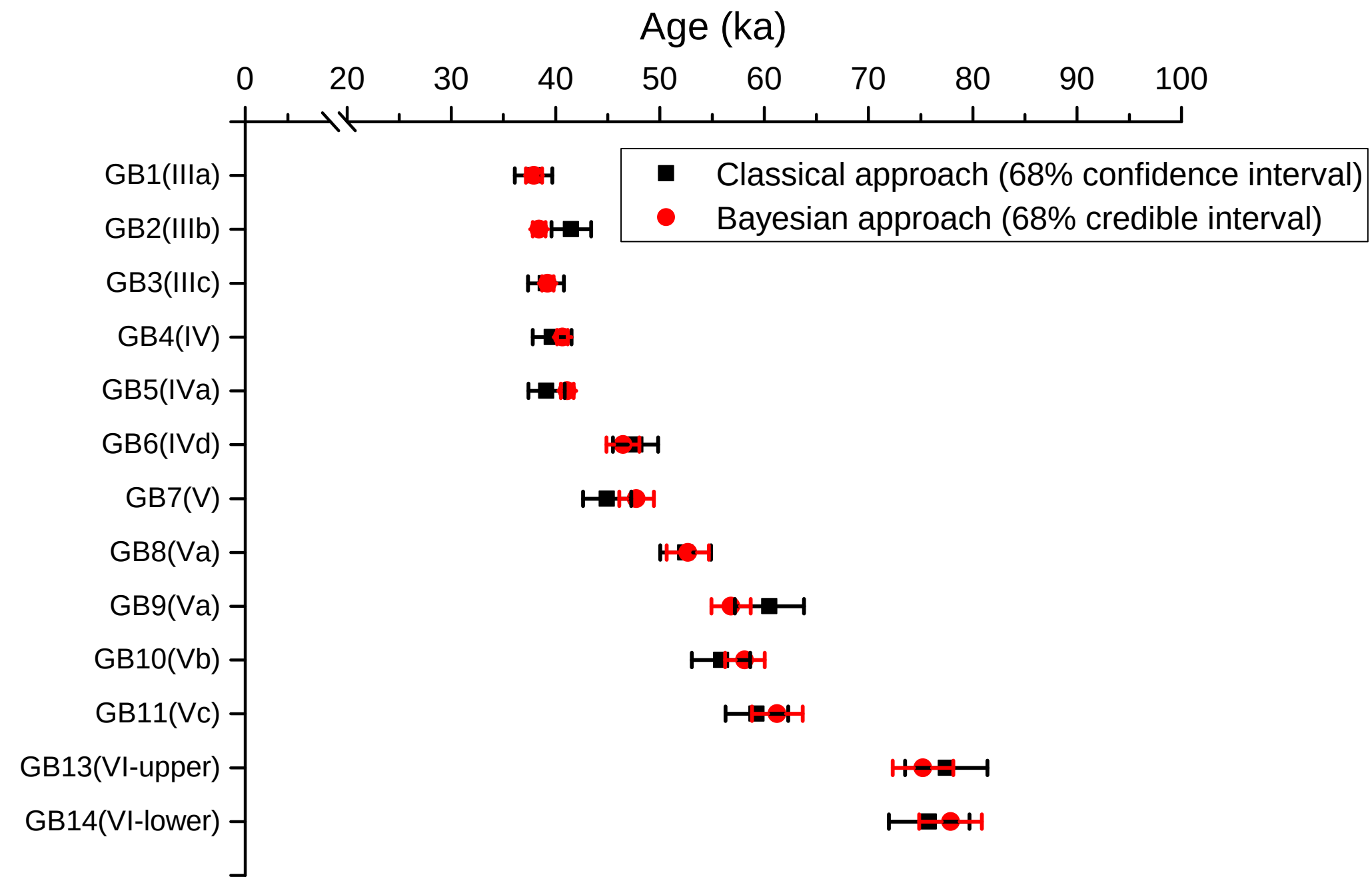
Age (ka)
0
20
30
40
50
60
70
80
90
100
GB1(IIIa)
GB2(IIIb)
GB3(IIIc)
GB4(IV)
GB5(IVa)
GB6(IVd)
GB7(V)
GB8(Va)
GB9(Va)
GB10(Vb)
GB11(Vc)
GB13(VI-upper)
GB14(VI-lower)
Classical approach (68% confidence interval)
Bayesian approach (68% credible interval)

**Table 1**

The radionuclide concentration derived by gamma-ray spectrometry.

| Sample name | K (%) | σ | U pre-Ra (ppm) | σ | U post-Ra (ppm) | σ | Th (ppm) | σ |
|---|---|---|---|---|---|---|---|---|
| GB1 | 1.01 | 0.02 | 1.51 | 0.11 | 1.33 | 0.03 | 2.80 | 0.06 |
| GB2 | 0.84 | 0.02 | 1.49 | 0.10 | 1.23 | 0.03 | 2.49 | 0.06 |
| GB3 | 0.84 | 0.02 | 1.66 | 0.09 | 1.68 | 0.03 | 2.58 | 0.05 |
| GB4 | 0.73 | 0.02 | 2.30 | 0.10 | 1.64 | 0.03 | 2.54 | 0.06 |
| GB5 | 0.75 | 0.02 | 2.23 | 0.11 | 2.01 | 0.03 | 2.47 | 0.06 |
| GB6 | 0.61 | 0.02 | 1.96 | 0.10 | 1.89 | 0.03 | 2.47 | 0.05 |
| GB7 | 0.61 | 0.02 | 2.48 | 0.11 | 1.30 | 0.03 | 2.19 | 0.06 |
| GB8 | 0.59 | 0.02 | 2.08 | 0.09 | 1.95 | 0.03 | 2.26 | 0.05 |
| GB9 | 0.56 | 0.02 | 2.26 | 0.10 | 2.06 | 0.03 | 2.24 | 0.05 |
| GB10 | 0.62 | 0.02 | 2.43 | 0.10 | 1.82 | 0.03 | 2.31 | 0.05 |
| GB11 | 0.49 | 0.01 | 2.24 | 0.09 | 2.15 | 0.03 | 1.96 | 0.04 |
| GB12 | 0.38 | 0.01 | 2.13 | 0.09 | 2.06 | 0.03 | 1.68 | 0.04 |
| GB13 | 0.40 | 0.01 | 2.59 | 0.09 | 1.99 | 0.03 | 1.70 | 0.04 |
| GB14 | 0.64 | 0.02 | 2.89 | 0.12 | 2.44 | 0.04 | 2.58 | 0.06 |

Abbreviation: σ = error-propagated uncertainty.

**Table 2**

The determined environmental dose rates.

| Sample name | Alpha-$D_r$ (Q) (Gy/ka) | σ | Alpha-$D_r$ (PM) (Gy/ka) | σ | Beta-$D_r$ (Gy/ka) | σ | Gamma-$D_r$ (Gy/ka) | σ | In situ gamma-$D_r$ (Gy/ka) | σ | Cosmic-$D_r$ (Gy/ka) | σ | Total-$D_r$ (Q) (Gy/ka) | σ | Total-$D_r$ (PM) (Gy/ka) | σ |
|---|---|---|---|---|---|---|---|---|---|---|---|---|---|---|---|---|
| GB1 | 0.04 | 0.01 | 0.14 | 0.02 | 0.89 | 0.05 | 0.46 | 0.02 | 0.49 | 0.03 | 0.11 | 0.01 | 1.55 | 0.06 | 1.81 | 0.07 |
| GB2 | 0.04 | 0.01 | 0.13 | 0.02 | 0.77 | 0.04 | 0.41 | 0.02 | 0.42 | 0.02 | 0.10 | 0.01 | 1.34 | 0.04 | 1.60 | 0.06 |
| GB3 | 0.05 | 0.01 | 0.15 | 0.02 | 0.80 | 0.04 | 0.44 | 0.02 | 0.44 | 0.02 | 0.10 | 0.01 | 1.40 | 0.04 | 1.67 | 0.06 |
| GB4 | 0.05 | 0.01 | 0.17 | 0.02 | 0.77 | 0.04 | 0.45 | 0.02 | 0.46 | 0.01 | 0.10 | 0.01 | 1.39 | 0.04 | 1.67 | 0.06 |
| GB5 | 0.06 | 0.01 | 0.17 | 0.03 | 0.80 | 0.04 | 0.45 | 0.02 | 0.46 | 0.02 | 0.10 | 0.01 | 1.42 | 0.04 | 1.71 | 0.06 |
| GB6 | 0.05 | 0.01 | 0.16 | 0.02 | 0.68 | 0.03 | 0.41 | 0.01 | 0.43 | 0.01 | 0.09 | 0.01 | 1.26 | 0.03 | 1.54 | 0.06 |
| GB7 | 0.05 | 0.01 | 0.15 | 0.02 | 0.67 | 0.03 | 0.40 | 0.02 | 0.40 | 0.03 | 0.09 | 0.01 | 1.23 | 0.05 | 1.50 | 0.07 |
| GB8 | 0.05 | 0.01 | 0.16 | 0.02 | 0.67 | 0.03 | 0.40 | 0.01 | 0.42 | 0.01 | 0.09 | 0.01 | 1.24 | 0.03 | 1.52 | 0.06 |
| GB9 | 0.05 | 0.01 | 0.17 | 0.03 | 0.67 | 0.03 | 0.41 | 0.02 | 0.40 | 0.03 | 0.09 | 0.01 | 1.22 | 0.05 | 1.51 | 0.07 |
| GB10 | 0.05 | 0.01 | 0.17 | 0.03 | 0.71 | 0.03 | 0.43 | 0.02 |  |  | 0.08 | 0.01 | 1.25 | 0.05 | 1.57 | 0.06 |
| GB11 | 0.05 | 0.01 | 0.17 | 0.03 | 0.62 | 0.03 | 0.39 | 0.01 |  |  | 0.08 | 0.01 | 1.16 | 0.04 | 1.43 | 0.06 |
| GB12 | 0.05 | 0.01 | 0.16 | 0.03 | 0.53 | 0.02 | 0.35 | 0.01 |  |  | 0.08 | 0.01 | 1.02 | 0.03 | 1.29 | 0.05 |
| GB13 | 0.05 | 0.01 | 0.16 | 0.03 | 0.54 | 0.03 | 0.36 | 0.02 |  |  | 0.08 | 0.01 | 1.04 | 0.04 | 1.31 | 0.06 |
| GB14 | 0.06 | 0.01 | 0.20 | 0.03 | 0.75 | 0.04 | 0.47 | 0.02 |  |  | 0.08 | 0.01 | 1.38 | 0.05 | 1.68 | 0.07 |

Abbreviations: Q = quartz; PM = polymineral; σ = error propagated uncertainty; $D_r$ = estimated dose-rate.

**Table 3**

The equivalent dose and corresponding ages in the classical approach.

| Sample name | $D_e$ (Q) (Gy) | SEM | Age (Q) (ka) | σ | $D_e$ (PM) (Gy) | SEM | Age (PM) (ka) | σ |
|---|---|---|---|---|---|---|---|---|
| GB1 | 59 | 1 | 38 | 2 | 68 | 1 | 37 | 2 |
| GB2 | 55 | 1 | 42 | 2 | 65 | 1 | 41 | 2 |
| GB3 | 55 | 1 | 39 | 2 | 69 | 2 | 42 | 2 |
| GB4 | 55 | 1 | 40 | 2 | 65 | 2 | 39 | 2 |
| GB5 | 55 | 1 | 39 | 2 | 68 | 2 | 40 | 2 |
| GB6 | 60 | 1 | 48 | 2 | 71 | 2 | 46 | 2 |
| GB7 | 55 | 1 | 45 | 2 | 67 | 2 | 45 | 2 |
| GB8 | 65 | 2 | 52 | 2 | 88 | 4 | 58 | 3 |
| GB9 | 74 | 2 | 61 | 3 | 90 | 3 | 60 | 4 |
| GB10 | 70 | 1 | 56 | 3 | 88 | 3 | 56 | 3 |
| GB11 | 69 | 1 | 59 | 3 | 87 | 5 | 60 | 4 |
| GB12 | — | — | — | — | 86 | 2 | 66 | 3 |
| GB13 | 80 | 2 | 77 | 4 | 102 | 4 | 77 | 5 |
| GB14 | 104 | 3 | 76 | 4 | 124 | 3 | 74 | 4 |

Abbreviations: $D_e$ = equivalent dose; SEM = standard error of the mean; σ = error propagated uncertainty; Q = quartz; PM = polymineral.